International Journal of Machine Tools & Manufacture 86 (2014) 18–33

Contents lists available at ScienceDirect

International Journal of Machine Tools & Manufacture

journal homepage: www.elsevier.com/locate/ijmactool

Critical cutting speed for onset of serrated chip flow in high speed machining

G.G. Ye [a,b], Y. Chen [a], S.F. Xue [b], L.H. Dai [a,*]

[a] State Key Laboratory of Nonlinear Mechanics, Institute of Mechanics, Chinese Academy of Sciences, Beijing 100190, China
[b] Department of Engineering Mechanics, College of Pipeline and Civil Engineering, China University of Petroleum, Shandong 266580, China

ARTICLE INFO

Article history:
Received 22 March 2014
Received in revised form
6 June 2014
Accepted 16 June 2014
Available online 23 June 2014

Keywords:
High speed machining
Serrated chip flow
Dimensional analysis
Shear banding

ABSTRACT

The transition of continuously smooth chip flow to periodically serrated chip flow as the cutting speed increasing is one of the most fundamental and challenging problems in high speed machining. Here, an explicit expression of the critical cutting speed for the onset of serrated chip flow, which is given in terms of material properties, uncut chip thickness and tool rake angle, is achieved based on dimensional analysis and numerical simulations. It could give reasonable predictions of the critical cutting speeds at which chips change from continuous to serrated for various metallic materials over wide ranges of uncut chip thickness and tool rake angle. More interestingly, it is found that, as the turbulent flow is controlled by the Reynolds number, the transition of the serrated chip flow mode is dominated by a Reynolds thermal number. Furthermore, the influences of material properties on the emergence of serrated chip flow are systematically investigated, the trends of which show good agreement with Recht's classical model.

1. Introduction

Cutting is a ubiquitous activity in daily life, science and technology [1,2]. The growing demand for enhancing production efficiency has stretched a rapid development of high speed machining (HSM) technology, which has many advantages such as high removal rates, low cutting forces, leading to excellent dimensional accuracy and surface finishing quality [3,4]. However, higher cutting speed usually renders the emergence of serrated chip flow [5], which ties up with decreased tool life, degradation of the surface finish and less accuracy in the machined part [6]. So, to predict the critical condition and especially the critical cutting speed for the onset of serrated chip flow could be of significant importance.

The mechanism for the onset of serrated chip flow has been extensively studied [7–12], and for most ductile metallic materials, the emergence of serrated chip flow is found be related to the thermoplastic shear instability occurred in the primary shear zone (PSZ) [8,9], which is often referred to the formation of adiabatic shear band [13–16]. And thus, considerable efforts have been carried out to focus on the adiabatic shear localization in the serrated chip formation process, and several classical theoretical models have been developed to predict the onset of serrated chip flow.

The first prediction for the emergence of serrated chip flow was provided by Recht [17]. He pointed out that when the tendency of the material in PSZ to harden with plastic deformation is overtaken by thermal softening effects, catastrophic shear occurs, and thus the serrated chip forms. A similar approach was proposed by von-Turkovich and Durham [18] to explain the transition of chip flow from continuous to serrated. It was assumed that such transition requires a maximum in the shear stress–shear strain curve. Hou and Komanduri [19] and Komanduri and Hou [20] extended Recht's classical model to predict the onset of shear instability. In their model, the possible sources of heat contributing toward the temperature rise are identified based on an analysis of the cyclic chip flow, and the temperature in the shear band was determined by using Jeager's classical methods. The shear stress in the shear band is calculated at the shear-band temperature and compared with the value of the shear strength of the bulk material at the preheating temperature. They stated that, once the shear stress in the shear band is less than or equal to the shear strength of the bulk material, shear localization is imminent.

The analytical model presented by Semiatin and Rao [21] is perhaps the first to provide a quantitative prediction of the critical speed at which the serrated chips are produced. Using the data available in the literature, the serrated flow is found to be imminent when the flow localization parameter (the ratio of the

* Corresponding author. Tel.: +86 10 82543958; fax: +86 10 82543977.
E-mail address: lhdai@lnm.imech.ac.cn (L.H. Dai).

http://dx.doi.org/10.1016/j.ijmachtools.2014.06.006
0890-6955/

normalized flow softening rate to the strain rate sensitivity) is equal to or greater than 5. This model could give reasonable predictions of the critical speeds for the emergence of serrated chip flow in machining of AISI 4340 and 1045 steels, but the predicted critical speeds for titanium were much higher than the experimental findings reported by Recht [17]. Later, Xie et al. [22,23] extended Semiatin and Rao's model to investigate the effect of cutting conditions on the onset of shear localization in metal cutting. In their work, the power law relation was used to describe the material plastic behavior, and Loewen and Shaw's model was applied to estimate the shear band temperature. And thus the flow localization parameter can be expressed in terms of associated cutting conditions and properties of the work material. Once the flow localization parameter surpasses the critical value which should be determined experimentally, the shear localization occurs.

By applying ideas from the theory of the formation of adiabatic shear band in torsion, Molinari and Dudzinski [24] derived the condition under which continuous chip flow becomes unstable. Soon after, Burns and Davies [25,26] introduced the concept of a local deformation zone to treat the tool, chip and workpiece as a coupling system. They derived the critical condition for the onset of serrated chip flow by solving the differential equations for the force balance and heat balance inside PSZ. And they pointed out that the emergence of serrated chip flow can be explained as a supercritical Hopf bifurcation phenomenon: the limit cycle of the nonlinear dynamic system of tool–chip–workpiece.

With considering the effect of strain gradient which becomes important in the case of shear localization, Aifantis and his coworkers [27,28] presented a method for thermo-viscoplastic instability in chip formation to describe the serrated chip flow. In their work, the shear deformation inside PSZ is treated as a simple shear. They carried out the perturbation analysis to predict the onset of serrated chip flow, and the relations for the shear band width and spacing were also established. Similarly, also by using perturbation analysis, some other adiabatic shear critical conditions were built by Li et al. [29], Ye et al. [30] and Ma et al. [31]. In these works, some specific effects of HSM were considered. Li et al. [29] considered the compressive stress applied on the shear plane, and the adiabatic shear is found to be favored by larger compression stress; In Ye et al.'s work [30], the material convection coursed by the high speed chip flow was taken into consideration, and the material convection is proposed to be negative for the shear localization; Ma et al. [31] established a general criterion for predicting the material instability under combined stresses loading, and applied it to the orthogonal cutting process. They stated that, once the plastic work of shear deformation is larger than one-third of that of stretching deformation, or is larger than four times of that of shrinking deformation, the shear located instability is imminent, and the serrated chip flow emerges.

At recent, Childs [32] predicted the onset of serrated chip flow by introducing a thermal number. He pointed out that once the thermal number achieves a critical number, the shear localization occurs. However, the critical thermal number depends on the material properties and tool rake angle, which should be determined by experimentations or numerical simulations.

Besides the theoretical analysis, the finite element (FE) method has also been widely used to predict the onset of serrated chip flow. Bäker et al. [33] and Bäker [34] predicted the serrated chip formation when cutting Ti–6Al–4V alloy by using ABAQUS. The distance criterion for chip separation was used in their model, and the general trends concerning serrated chip flow were deduced related with the work material behavior. Rhim and Oh [35] proposed a new flow stress model which takes into account dynamic recrystallization to predict the adiabatic shear localization during cutting AISI 1045 steel. It was found that the serrated chips can be predicted by using the rigid plastic FE simulation together with the new flow stress model. Later, Arrazola et al. [36,37] modeled the 2D orthogonal cutting by using the Arbitrary Lagrangian Eulerian formulation proposed in ABAQUS/Explicit. The sensitivity of serrated chip prediction to the cutting speed and material input parameters was systematically analyzed. More recently, an adaptive numerical methodology was developed by Issa et al. [38] to predict the thermo-mechanical field localization in orthogonal cutting AISI 4340 stainless steel. In their work, the main thermo-mechanical phenomena such as the nonlinear isotropic and kinematic hardening with thermal and ductile damage effects were taken into account. And the effects of uncut chip thickness, initial temperature, friction coefficient and work ductility on the adiabatic shear localization were investigated. Using the Johnson–Cook damage criterion for chip separation and the modified Zorev model for tool–chip friction description, Duan and Zhang [39,40] developed a FE method to precisely predict the onset and the formation of serrated chip flow without artificial assumptions. And the effects of the cutting conditions were also investigated. Miguélez et al. [41] performed the FE simulations to predict the shear localization involved in high speed machining of Ti–6Al–4V in a wide range of cutting speeds and feed rates. The effects of some material parameters on shear flow stability were investigated. It states that, the strain hardening exponent has a stabilizing effect, and increasing the initial yield stress has a destabilizing effect on the onset of serrated chip flow.

It should be pointed out that, all these fantastic pioneer works give important clues for the understanding of the physics and mechanics of serrated chip flow. And for most of the theoretical instability criterions, they may give universal descriptions for the onset of serrated chip flow, since they were achieved based on the universal equations controlling the PSZ deformation. However, additional complex numerical calculations are usually required to predict the critical cutting speed at which the chip flow changes from continuous to serrated. As for the FE simulations, the onset of the serrated chip flow can be precisely predicted. However, it should be pointed out that, in cutting process the work materials differ widely in their ability to deform plastically, to fracture and to sustain tensile/compressive stresses [42], thus the onset of serrated chip flow could have strong dependence on the work material. But for most of the FE analyses, they are usually focusing on a certain work material. Moreover, though some fantastic pioneer FE analyses have qualitatively investigated the effects of material properties and cutting conditions on the onset of serrated chip flow, the quantitative relationship has not been established. And the universal explicit expression of the critical cutting speed for the onset of serrated chip flow is still unavailable.

In this work, high speed cuttings of various metallic materials were carried out over wide ranges of cutting speeds. Based on the experimental results, the dimensional analysis and numerical simulations were applied to predict the critical cutting speed at which the serrated chip flow is produced. The universal expression of the critical cutting speed for cutting metallic material by using sharp tools is given in terms of the material properties, uncut chip thickness and tool rake angle. It is demonstrated here that once the Reynolds thermal number achieves a critical value that dominated by the work material properties, the serrated chip flow emerges. This shows striking parallels to the turbulent flow which takes place as the Reynolds number surpasses a critical value determined by the fluid properties. Furthermore, the influences of the material properties on the onset of serrated chip flow are investigated systematically, the trends of which are in accordance with Recht's classical criterion.

Table 1
Cutting parameters.

Rake angle ω	Clearance angle	Tool edge radius	Uncut chip thickness	Cutting speed
0°	7°	0.01 mm	100 μm	0.05–90 m/s

2. Experimental

To investigate the universal behavior existing in metal cutting, five typical metallic materials, which are widely employed in automotive, aerospace, and other industrial applications, are chose as work materials. They includes nickel-base superalloy (IN 718), titanium alloy (Ti–6Al–4V), steel (AISI 4340), aluminum alloy (Al 7075) and copper. These five materials, from easy to difficult-to-cut, have great differences in their thermo-physical properties. They cover a wide range of thermal diffusion, from $3.0\times10^{-6}\,m^2\,s^{-1}$ for IN 718 to $116\times10^{-6}\,m^2\,s^{-1}$ for copper.

Cutting experiments were carried out over a wide range of cutting speeds from 0.05 m/s to 90 m/s by using computer-controlled lathe (0.05–5 m/s) and light-gas gun based device (5–90 m/s). The details of the light-gas gun based experimental device can be found in Ref. [30]. Uncoated P10 carbide tools were applied, and new cutting inserts were used for each test to limit the influence of tool wear. Other test conditions can be found in Table 1.

After cutting, the chips were collected and embedded into resin. The cross section was mechanically polished and then etched. Microscopic observations were carried out to examine the influence of cutting speed on the chip flow mode.

3. Results

The flow pattern of chip flow evolves with cutting speed for Al 7075, AISI 4340 steel, Ti–6Al–4V and IN 718 are shown in Fig. 1. It should be pointed out that, the chip flow of copper is all continuously smooth in the applied cutting speed range (3–89 m/s), so is not shown here.

For the work materials Al 7075, AISI 4340 steel, IN 718 and Ti–6Al–4V, there exists a distinct transition from continuously smooth flow to periodically serrated flow with cutting speed increasing. And the critical cutting speed corresponding to such transition exhibits a strong material dependency. Moreover, by comparing the critical cutting speeds for these four work materials, it is found that the transition from continuously smooth to periodically serrated chip flow seems to be favored by decreasing in material thermal diffusion. About how the thermal diffusion and other material properties affect the onset of serrated chip flow will be systematically discussed in the next section.

The chip flow is continuously smooth at lower speeds. The chip flow is smooth, and the flow motion is homogenous as all crystal particles are elongated uniformly in a same direction. However, as the cutting speed increases, the continuously smooth chip flow becomes unsettled. Highly localized shear bands emerge because the smooth chip flow is not sufficient to dissipate the energy through homogeneous plastic flow. The steady chip flow is broken by the periodic emergence of shear bands, and the smooth free surface turns out to be fluctuant, thus a serrated chip flow forms (see Fig. 2a). From Fig. 2a it can be found that the serrated flow motion is quite inhomogenous since the crystal particles inside the shear bands are elongated seriously along the shear direction while those outside the shear bands remain almost undeformed. The widely observed shear bands between the saw-teeth indicate that the serrated chip flow in HSM is closely related to the repeated shear banding.

Moreover, the examination of the free surface of the serrated chip flow reveals a fine distributed lamellar structure (see Fig. 2b). The shear surfaces of each adjacent lamella show severe elongated dimple structures. This dimple structure is the most significant feature of adiabatic shear fracture, which is formed under the effect of shear stress when shear bands had been produced [43]. The obviously observed elongated dimple structure further demonstrates that the serrated chip flow is ascribed to repeated shear banding rather than periodic cracking. Therefore, we can take the condition at which the shear bands just regularly emerge in the chip as the critical condition for the onset of serrated chip flow.

4. Universal expression of the critical cutting speed for the onset of serrated chip flow

From the experimental results we have known that the onset of serrated chip flow has a strong dependency on the work material. To clarify the link between the onset of serrated chip flow and the material properties, the dimensional analysis is carried out.

A special attention is accorded to the dependence of the critical cutting speed for the onset of serrated chip flow (V_c) with respect to the material parameters and cutting conditions. Generally, V_c depends on the following terms:

(a) The cutting conditions and tool–chip interface characteristics: uncut chip thickness b; tool rake angle ω; tool edge radius r; tool–chip friction coefficient μ.
(b) The physical and mechanical properties of the work material: mass density ρ, elastic modulus E, Poisson's ratio ν, thermal parameters (thermal diffusion λ, heat capacity c and Taylor–Quinney coefficient β which defines the fraction of plastic work converted into heat) and the parameters of the plastic constitutive equation.

Usually, for most metal materials, the Johnson–Cook (J–C) law is adopted to describe the coupling effects of strain hardening, rate hardening and thermal softening on plastic flow:

$$\sigma=(A+B\varepsilon^n)\left[1+C\ln\left(\frac{\dot\varepsilon}{\dot\varepsilon_0}\right)\right]\left[1-\left(\frac{T-T_0}{T_m-T_0}\right)^m\right] \tag{1}$$

where σ is the plastic stress, ε is strain, $\dot\varepsilon$ is strain rate, and T is temperature. In Eq. (1), A is the initial yield stress, B the hardening modulus, n the work-hardening exponent, C the strain rate dependency coefficient, $\dot\varepsilon_0$ the reference strain rate, m the thermal softening coefficient, T_0 the reference temperature and T_m is the melting temperature.

The values of J–C parameters and other thermo-mechanical properties used to describe the behavior of IN 718, Ti–6Al–4V, AISI 4340 steel, Al 7075 and copper are specified in Tables 2 and 3 [35–51].

Thus, the critical cutting speed V_c is function of b, ω, r, μ, ρ, E, ν, λ, c, β, A, B, n, C, $\dot\varepsilon_0$, m, T_0 and T_m. Using the Vashy–Buckingham theorem, the following relationship is obtained:

$$\overline{V}_c=f(\overline{\lambda},\overline{E},\overline{A},\overline{B},\overline{T}_m,\overline{\dot\varepsilon}_0,C,m,n,\omega,r,\mu,\nu,\beta) \tag{2a}$$

where

$$\overline{V}_c=V_c/(cT_0)^{1/2},\ \overline{\lambda}=\lambda^2/cT_0b^2,\ \overline{E}=E/\rho cT_0,\ \overline{A}=A/\rho cT_0,\ \overline{B}=B/\rho cT_0,$$

$$\overline{T}_m=T_m^*/T_0,\ \overline{\dot\varepsilon}_0=\dot\varepsilon_0 b/(cT_0)^{1/2} \tag{2b}$$

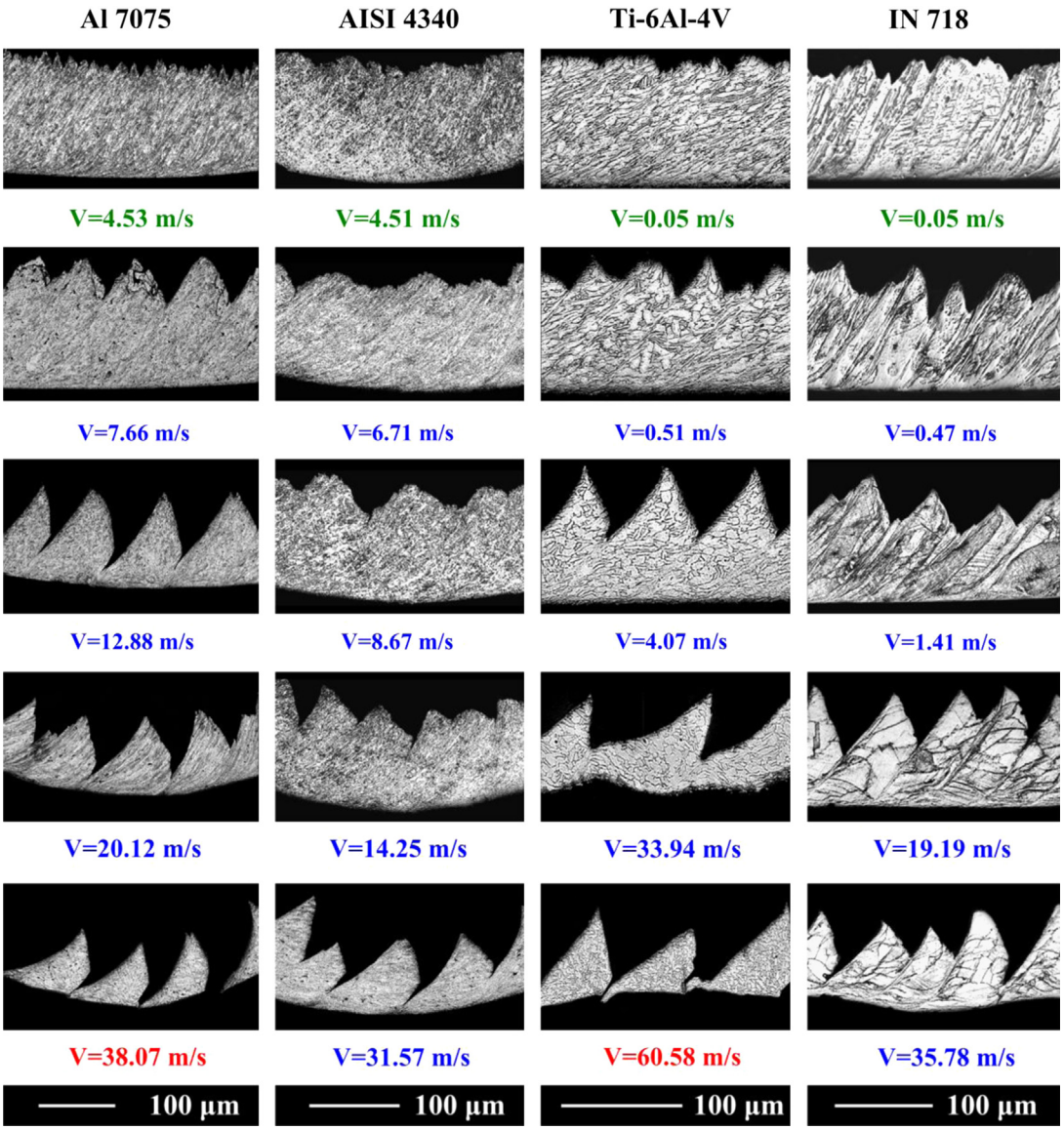

Fig. 1. Chip flow pattern evolves with cutting speed for Al 7075, AISI 4340, Ti–6Al–4V and IN 718.

where $T_m^* = T_m - T_0$. Here, the dimensionless velocity $\overline{V}_c$, which can be given as $\sqrt{\rho V_c^2/\rho c T_0}$, reflects the ratio of the kinetic energy of external loading to the initial thermal energy. And the dimensionless numbers $\overline{\lambda}$ and $\overline{E}$ reflect the ratio of the energy consumed in thermal diffusion and the energy stored in elastic deformation to the energy required for initial thermal heating, respectively. $\overline{A}$ and $\overline{B}$ characterize respectively the internal heating due to plastic deformation in yielding and strain hardening process.

For simplicity, here Poisson's ratio ν, tool edge radius r, tool–chip friction coefficient μ and the Taylor–Quinney coefficient β are kept as constant ($\nu=0.3$; $r=0^\circ$; $\mu=0.3$; $\beta=0.9$). Therefore, by omitting the parameters that are only dependent upon ν, r, μ, and β, Eq. (2) can be written as

$$\overline{V}_c = f(\overline{\lambda}, \overline{E}, \overline{A}, \overline{B}, \overline{T}_m, C, \overline{\varepsilon}_0, m, n, \omega) \tag{3}$$

To determine the functional dependence, it is necessary to capture the critical cutting speeds for any combination of these dimensionless parameters. In this work, the experimentally-validated finite element model is developed to obtain the critical cutting speeds for given material parameters and cutting conditions. The details of the numerical simulation can be found in the Appendix A.

It should be pointed out that, for the continuous chip flow, the cutting force is almost constant after the cutting process stabilized. But for the serrated flow, a cyclic cutting force is produced, and the perturbation of the cutting force rises with increasing the cutting speed. Here, to define the critical cutting speed, we assumed that, when the fluctuation of the cutting force ($\Delta F_c/F_{aver}$) achieves 10%, the transiton from continuous chip flow to serrated chip flow is regared to be taken place, and the correspondind cutting speed is set as V_c. At this condition, the shear bands just regularly emerge in the chip, and the saw-teeth becomes visible, as shown in Fig. 3. From the HSM experiments we have known that, the serrated chip flow results from repeated shear banding. Thus we can take the condition at which the shear bands just regularly emerge in the chip as the critical condition for the onset of serrated chip flow. So, we have reasons to believe that the critical cutting speed defined above is reasonalbe.

For any combination of the dimensionless parameters, we can get the corresponding $\overline{V}_c$ by using FEM simulations. Thus, by varying any one of the non-dimensional parameters while keeping the others constant, we can get the evolution rule of $\overline{V}_c$ with such non-dimensional parameter.

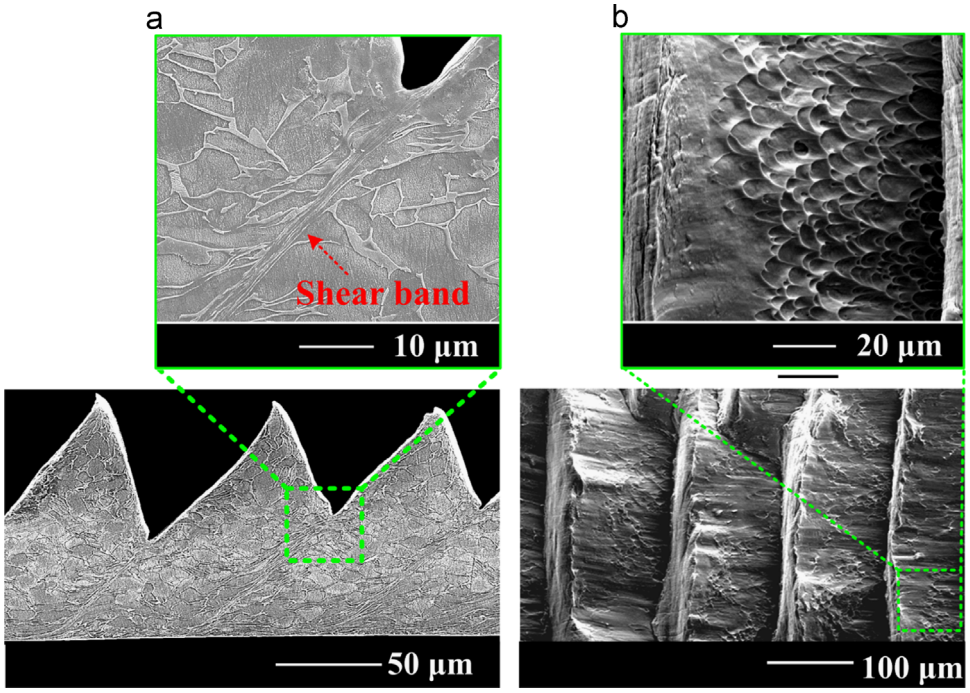

Fig. 2. Microstructure of (a) chip morphology and (b) chip free surface for Ti–6Al–4V (V=4.07 m/s).

Table 2
The values of the J–C parameters.

Material	A (MPa)	B (MPa)	C	n	m	$\dot{\varepsilon}_0$ (s^{-1})	T_m (K)	T_0 (K)
Copper [44]	100	292	0.025	0.31	1.09	1	1356	300
Al 7075 [45]	546	678	0.024	0.71	1.56	1	893	300
AISI 4340 [46]	792	510	0.014	0.26	1.03	1	1793	300
Ti–6Al–4V [47]	783	497	0.028	0.28	1.00	1×10^{-5}	1880	300
IN 718 [48]	1350	1139	0.014	0.65	1.00	1	1570	300

Table 3
Mechanical properties and parameters.

Parameters	Copper [44]	Al 7075 [49]	AISI 4340 [50]	Ti–6Al–4V [51]	IN 718 [48]
E (GPa)	129	71	200	105	210
ρ (kg m^{-3})	8960	2770	7860	4430	8200
λ (10^{-6} m^2 s^{-1})	116	53	13	3	3
(c) (J kg^{-1} K^{-1})	383	885	473	520	435

For the non-dimensional parameters $\overline{\lambda}$, $\overline{E}$, $\overline{A}$, $\overline{B}$, $\overline{T}_m$ and $\overline{\dot{\varepsilon}}_0$, they contain several variable parameters. It can be found that λ, E, A, B, T_m and $\dot{\varepsilon}_0$ are the independent variables for $\overline{\lambda}$, $\overline{E}$, $\overline{A}$, $\overline{B}$, $\overline{T}_m$ and $\overline{\dot{\varepsilon}}_0$, respectively. And ρ, c, T_0 and b are their public variables. Here, we changed the values of the independent variables λ, E, A, B, T_m and $\dot{\varepsilon}_0$ to vary respectively the $\overline{\lambda}$, $\overline{E}$, $\overline{A}$, $\overline{B}$, $\overline{T}_m$ and $\overline{\dot{\varepsilon}}_0$. As thus, when varying these multi-variable dimensionless parameters, the other dimensionless parameters can be kept constant. Also, we can change the values of the public variables. But it should be noticed that, when varying any one of the multi-variable dimensionless parameters by change the values of the public variables, it must change simultaneously the value of the independent variables of the other multi-variable dimensionless parameters to keep them constant.

To investigate the changing tendencies of $\overline{V}_c$ with $\overline{\lambda}$, $\overline{E}$, $\overline{A}$, $\overline{B}$, $\overline{T}_m$ $\overline{\dot{\varepsilon}}_0$, C, n, m and ω, 10 sets of simulations were applied. The corresponding values of the independent/public variables for each set are given in Table 4. Here, the room temperature T_0 is set to be 300 K as constant for simplicity. Moreover, to achieve universal evolution rules of $\overline{V}_c$, we investigate the changing tendencies of $\overline{V}_c$ with each dimensionless parameter for 3 different combinations of the other dimensionless parameters, as shown in Table 4.

By investigating the evolution rules of $\overline{V}_c$ with $\overline{\lambda}$, $\overline{E}$, $\overline{A}$, $\overline{B}$, $\overline{T}_m$ $\overline{\dot{\varepsilon}}_0$, C, n, m and ω, we get that

$$\overline{V}_c \propto f_1(\omega) = e^{1.5\ \tan(45^\circ+\omega)-1.5} \tag{4a}$$

$$\overline{V}_c \propto f_2(\overline{\lambda}) = \overline{\lambda}^{0.5} \tag{4b}$$

$$\overline{V}_c \propto f_3(\overline{E}) = \overline{E}^{0.4} \tag{4c}$$

$$\overline{V}_c \propto f_4(n) = e^{8.5n} - 1 \tag{4d}$$

$$\overline{V}_c \propto f_5(\overline{A}, \overline{B}) \tag{4e}$$

$$\overline{V}_c \propto f_6(C, \overline{\dot{\varepsilon}}_0) \tag{4f}$$

$$\overline{V}_c \propto f_7(\overline{T}_m, m) \tag{4g}$$

The dimensionless cutting speed $\overline{V}_c$ evolves with ω, $\overline{\lambda}$, $\overline{E}$, and n for different combinations of other dimensionless parameters are shown in Fig. 4.

It can be found that, the evolution rules of $\overline{V}_c$ with ω, $\overline{\lambda}$, $\overline{E}$, and n are independent on the other parameters, while $\overline{A}$ and $\overline{B}$, C and $\overline{\dot{\varepsilon}}_0$, $\overline{T}_m$ and m have coupling effects on the evolution rules of $\overline{V}_c$. It should be noticed that, both $\overline{A}$ and $\overline{B}$ reflect the internal heating of the work material, C and $\overline{\dot{\varepsilon}}_0$ control together the material strain rate hardening, and the material thermal softening is dominated by both $\overline{T}_m$ and m. This may raise the possibility that $\overline{A}$ and $\overline{B}$, C and $\overline{\dot{\varepsilon}}_0$, $\overline{T}_m$ and m are coupled with each other.

According to Eqs. (4a)-(4g), the dimensionless critical cutting speed $\overline{V}_c$ can be given as

$$\overline{V}_c = C_0 f_1(\omega) f_2(\overline{\lambda}) f_3(\overline{E}) f_4(n) f_5(\overline{A}, \overline{B}) f_6(C, \overline{\dot{\varepsilon}}_0) f_7(\overline{T}_m, m) \tag{5}$$

where the expressions of f_1, f_2, f_3 and f_4 were given in Eqs. (4a)–(4d), C_0 is a constant coefficient, and all the constant coefficients of the equations f_5, f_6 and f_7 are equaled to 1.

To get the value of C_0 and to achieve the expressions of f_5, f_6 and f_7, six additional sets of simulations were carried out (see Table 5).

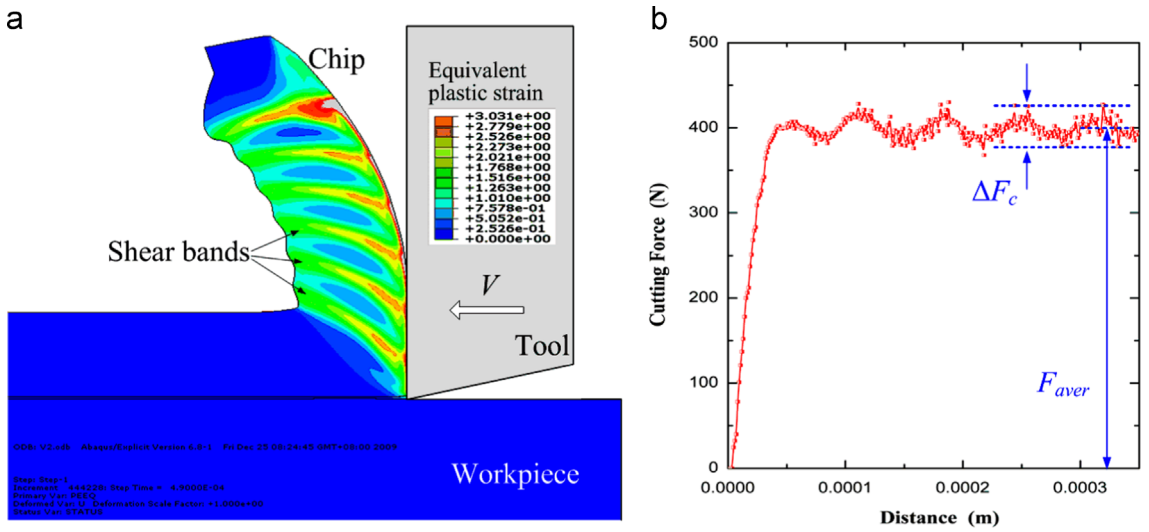

Fig. 3. (a) Simulated chip morphology and (b) the corresponding cutting force at the critical condition for the onset of serrated chip flow.

Based on the numerical fitting method, we selected carefully the function forms of f_5, f_6 and f_7 to fit all the 16 sets of simulation results obtained based on Tables 4 and 5 (about 520 points), and finally get that

$$f_5(\overline{A},\overline{B}) = (\overline{A}+\overline{B}/3)^{-4.8} \tag{6a}$$

$$f_6(C,\dot{\overline{\varepsilon}}_0) = C^{-1.34-0.02\ \log\ \dot{\overline{\varepsilon}}_0} \tag{6b}$$

$$f_7(\overline{T}_m, m) = \overline{T}_m{}^{4.2} m^{\Lambda} \tag{6c}$$

where

$$\Lambda = 6(\rho c \overline{T}_m T_0/10^{10}\ \mathrm{J})^{1.5} \tag{6d}$$

And a unique constant coefficient $C_0 = 2.1\times10^{-6}$ is achieved.

The evolution of $\overline{V}_c$ as functions of $\overline{A}$ and $\overline{B}$, C and $\dot{\overline{\varepsilon}}_0$, $\overline{T}_m$ and m are respectively shown in Figs. 5–7. It is obvious that, $\overline{V}_c$ is linearly proportional to $(\overline{A}+\overline{B}/3)^{-4.8}$, $C^{-1.34-0.02\ \ln\ \dot{\overline{\varepsilon}}_0}$ and $\overline{T}_m{}^{4.2} m^{\Lambda}$, respectively.

As thus, the explicit expression of the critical cutting speed can be given by

$$\overline{V}_c = \Gamma\Phi\times\overline{\lambda}^{0.5} \tag{7a}$$

where

$$\Phi = e^{1.5\ \tan(45^0+\omega)-1.5} \tag{7b}$$

$$\Gamma = 2.1\times10^{-6} \times\overline{E}^{0.4}(\overline{A}+\overline{B}/3)^{-4.8}(e^{8.5n}-1)C^{-1.34-0.02\ \log\ \dot{\overline{\varepsilon}}_0}\overline{T}_m{}^{4.2} m^{6\Lambda^{1.5}} \tag{7c}$$

Here the dimensionless number Φ and Γ are determined by the tool rake angle and material properties, respectively.

By using Eq. (7), all the 16 sets of simulated data can be well fitted. It should be noticed that, the constant coefficients of the fitted lines plotted in Figs. 4–7 are all material dependent. However, all the constant coefficients for the fitted lines are in accordance with the values calculated from Eq. (7). For example, for the curve $\overline{V}_c-\overline{E}$ plotted in Fig. 4c, the constant coefficient of the fitted line for Ti–6Al–4V is 1.9×10^{-5}. And according to Eq. (7), a same constant coefficient $C' = C_0 f_1 f_2 f_4 f_5 f_6 f_7 = 1.9\times10^{-5}$ is obtained. Thus, from Figs. 4–7 it can be found that, the expression of the critical cutting speed for the onset of serrated chip flow given in Eq. (7) is universal for all the 520 simulated results.

And the 16 sets of numerical simulations cover very wide ranges of material properties and cutting conditions, which can be listed as follows:

$1\times10^{-6}\le\lambda\le1\times10^{-3}$ m^2/s;	$50\le E\le300$ GPa;	$100\le A\le1400$ MPa;
$00\le B\le1400$ MPa;	$0.1\le n\le1$;	$0.005\le C\le0.05$;
$10^{-5}\le\dot{\varepsilon}_0\le10^{5}$ s^{-1};	$0.5\le m\le2$;	$700\le T_m\le2300$ K;
$2500\le\rho\le9000$ kg/m^3;	$200\le c\le1000$ J/kg K;	$50\le b\le400$ μm;
$-15^\circ\le\omega\le15^\circ$.		

It can be noticed that, the properties for most metallic materials are within the ranges listed above. And in metal machining, the commonly applied values for the uncut chip thickness and tool rake angle are almost within the ranges listed above. So, the explicit expression of the critical cutting speed given in Eq. (7), which is achieved based on these simulations, can be regarded as universal for most commonly used metallic materials.

Rearranging the functional dependence (7a), the explicit expression of the critical cutting speed for the onset of serrated chip flow in terms of material properties, uncut chip thickness and tool rake angle can be further given by

$$\mathrm{Pe}_c = \Gamma\Phi \tag{8}$$

where $\mathrm{Pe}_c = V_c b/\lambda$ is a critical Péclect number.

Noticing that, the transition of the chip flow from continuously smooth to periodically serrated is favored by increasing in cutting speed. Thus, from Eq. (8) the critical criterion for the onset of serrated chip flow can be given as

$$\mathrm{Pe}/\Gamma\Phi > 1 \tag{9}$$

where $\mathrm{Pe} = Vb/\lambda$ is a Péclect number, which is also called as Reynolds thermal number [52] or thermal number [32], representing the ratio of transit time to relaxation time. In high speed cutting, there is no sufficient time for effective heat diffusion to take place. The heat stays where it is generated, and thus the serrated chip flow forms. It is found that this condition usually occurs when Pe is large [53].

The criterion (9) indicates that, once the ratio of the external loading to the thermal diffusion (Reynolds thermal number Pe) achieves a critical value that dominated by the material properties,

Table 4
Simulation conditions.

Set number	Variable parameter	The combination of other dimensionless parameters										ω (deg)	Values of variables	Data number
		Material	$\bar{\lambda}\times10^{-6}$	$\bar{E}$	$\bar{A}$	$\bar{B}$	n	$C\times10^{-2}$	$\bar{\varepsilon}_0$	$\bar{T}_m$	m			
1	ω	Al 7075	1.1	97	0.7	0.9	0.71	2.4	1.9×10^{-7}	2.0	1.56	–	ω (deg)= −15, −10, −5,0,5,10,15.	3∗7=21
		AISI 4340	1.2	179	0.7	0.5	0.26	1.4	2.7×10^{-7}	5.0	1.03			
		Ti–6Al–4V	5.8	152	1.1	0.7	0.28	2.8	2.5×10^{-12}	5.3	1.00			
2	$\bar{\lambda}$	Al 7075	–	97	0.7	0.9	0.71	2.4	1.9×10^{-7}	2.0	1.56	0	λ=1, 5, 10, 50, 100, 200×10^{-6} m^2 s^{-1}; or	3∗14=42
		AISI 4340	–	179	0.7	0.5	0.26	1.4	2.7×10^{-7}	5.0	1.03		b=50, 100, 200, 300, 400 μm; or	
		Ti–6Al–4V	–	152	1.1	0.7	0.28	2.8	2.5×10^{-12}	5.3	1.00		c=200,600,1000 J kg^{-1} K^{-1}.	
3	$\bar{E}$	Al 7075	1.1	–	0.7	0.9	0.71	2.4	1.9×10^{-7}	2.0	1.56	0	E=50, 100, 150, 200, 250, 300 GPa; or	3∗12=36
		AISI 4340	1.2	–	0.7	0.5	0.26	1.4	2.7×10^{-7}	5.0	1.03		ρ=2500, 5000, 9000 kg m^{-3}; or c=200,	
		Ti–6Al–4V	5.8	–	1.1	0.7	0.28	2.8	2.5×10^{-12}	5.3	1.00		600, 1000 J kg^{-1} K^{-1}.	
4	$\bar{A}$	Al 7075	1.1	97	-	0.9	0.71	2.4	1.9×10^{-7}	2.0	1.56	0	A=100,200,400,800,1400 MPa; or ρ=2500,	3∗11=33
		AISI 4340	1.2	179	-	0.5	0.26	1.4	2.7×10^{-7}	5.0	1.03		5000, 9000 kg m^{-3}; or c=200, 600,	
		Ti–6Al–4V	5.8	152	–	0.7	0.28	2.8	2.5×10^{-12}	5.3	1.00		1000 J kg^{-1} K^{-1}.	
5	$\bar{B}$	Al 7075	1.1	97	0.7	-	0.71	2.4	1.9×10^{-7}	2.0	1.56	0	B=100,200,400,800,1400 MPa; or ρ=2500,	3∗11=33
		AISI 4340	1.2	179	0.7	-	0.26	1.4	2.7×10^{-7}	5.0	1.03		5000, 9000 kg m^{-3}; or c=200, 600,	
		Ti–6Al–4V	5.8	152	1.1	-	0.28	2.8	2.5×10^{-12}	5.3	1.00		1000 J kg^{-1} K^{-1}.	
6	n	Al 7075	1.1	97	0.7	0.9	–	2.4	1.9×10^{-7}	2.0	1.56	0	n=0.1, 0.2, 0.3, 0.4, 0.5, 0.6, 0.7, 0.8, 0.9, 1.0.	3∗10=30
		AISI 4340	1.2	179	0.7	0.5	–	1.4	2.7×10^{-7}	5.0	1.03			
		Ti–6Al–4V	5.8	152	1.1	0.7	–	2.8	2.5×10^{-12}	5.3	1.00			
7	C	Al 7075	1.1	97	0.7	0.9	0.71	-	1.9×10^{-7}	2.0	1.56	0	C=0.005, 0.01, 0.015, 0.02, 0.025, 0.03, 0.035,	3∗10=30
		AISI 4340	1.2	179	0.7	0.5	0.26	-	2.7×10^{-7}	5.0	1.03		0.04, 0.045, 0.05.	
		Ti–6Al–4V	5.8	152	1.1	0.7	0.28	-	2.5×10^{-12}	5.3	1.00			
8	$\bar{\varepsilon}_0$	Al 7075	1.1	97	0.7	0.9	0.71	2.4	–	2.0	1.56	0	$\dot{\varepsilon}_0=1\times10^{-5}$, 1×10^{-3}, 1, 1×10^{3}, 1×10^{5}; or	3∗11=33
		AISI 4340	1.2	179	0.7	0.5	0.26	1.4	–	5.0	1.03		b=50, 200, 400 μm; or	
		Ti–6Al–4V	5.8	152	1.1	0.7	0.28	2.8	–	5.3	1.00		c=200,600,1000 J kg^{-1}K^{-1}.	
9	$\bar{T}_m$	Al 7075	1.1	97	0.7	0.9	0.71	2.4	1.9×10^{-7}	–	1.56	0	T_m=700, 900, 1100, 1300, 1500, 1700, 1900,	3∗9=27
		AISI 4340	1.2	179	0.7	0.5	0.26	1.4	2.7×10^{-7}	–	1.03		2100, 2300 K.	
		Ti–6Al–4V	5.8	152	1.1	0.7	0.28	2.8	2.5×10^{-12}	–	1.00			
10	m	Al 7075	1.1	97	0.7	0.9	0.71	2.4	1.9×10^{-7}	2.0	–	0	m=0.50, 0.75, 1.00, 1.25, 1.50, 1.75, 2.00.	3∗7=21
		AISI 4340	1.2	179	0.7	0.5	0.26	1.4	2.7×10^{-7}	5.0	–			
		Ti–6Al–4V	5.8	152	1.1	0.7	0.28	2.8	2.5×10^{-12}	5.3	–			

the serrated chip flow occurs. This shows striking analogy to the turbulent flow which takes place as the ratio of external loading to the viscous diffusion (Reynolds number Re) is up to a critical value that determined by the fluid properties. It is demonstrated that the continuous–serrated transition of the chip flow is controlled by the Reynolds thermal number as the laminar–turbulent transition of the fluid is dominated by the Reynolds number. It should be pointed out that, after the chip separates from the work material, it flows along the tool surface as the fluid flowing in a free surface water channel. The sticking friction takes place along the tool–chip interface [54,55], making the chip flow velocity increase gradually in a thin layer near the tool surface, which is quite similar to that in the fluid boundary layer. This may raise the possibility that similar dimensionless numbers exist for describing the onset of serrated chip flow in HSM and the emergence of turbulence in fluid boundary layer.

The evolution of $\mathrm{Pe}/\Gamma\Phi$ with Pe/Φ for various work materials are plotted in Fig. 8. In this figure, the solid and hollow patterns indicate that the chips obtained from corresponding cutting experiments are continuous and serrated, respectively. Some other published experimental data [30,32,56–70] are also given in this figure to validate the criterion (9). It can be noticed from Fig. 8 that, the serrated and continuous chip flow respectively fall in the zone of $\mathrm{Pe}/\Gamma\Phi>1$ and $\mathrm{Pe}/\Gamma\Phi<1$. And the transition of the flow pattern from continuous to serrated almost takes place around $\mathrm{Pe}/\Gamma\Phi=1$. In Fig. 8, the uncut chip thickness varies from 35 μm to 500 μm, and the tool rake angel is in the range of $-6^\circ\sim17.5^\circ$. And the work materials involve copper, aluminum alloys (Al 7075 and Al 2024), steels (AISI 4340 and AISI 4045), titanium alloy (Ti–6Al–4V) and nickel-base superalloy (IN 718). These materials have great differences in their physical and mechanical properties. It implies that the explicit expression (7a–c) and criterion (9) are universal, which can be used to predict the onset of serrated chip flow for various metallic materials over wide ranges of uncut chip thickness and tool rake angle.

More interestingly, after the serrated chip forms, there exists a scaling law between the serration spacing and the Reynolds thermal number, as shown in Fig. 9. Here, for the experimental results obtained in Section 3, we measured the total spacing of 10 randomly selected adjacent serrations for each serrated chip, and the average spacing is set to be the serration spacing. It can be found from Fig. 9 that all the data for IN 718, Ti–6Al–4V, AISI 4340 steel and Al 7075 can be fitted by a universal straight line with a slope about $-1/4$. Thus, the serration spacing, which is one of the most important parameters characterizing the serrated chip, follows a power low dependence on the Reynolds thermal number as $L\propto\mathrm{Pe}^{-1/4}$. It shows clearly that the Reynolds thermal number controls not only the initiation but also the evolution of the serrated chip flow. The Reynolds thermal number plays a major important role in the high speed machining of metallic materials.

5. The influence of material properties on the onset of serrated chip flow

5.1. Recht's instability criterion

To better investigate and understand the influence of material properties on the onset of serrated chip flow, let us first introduce

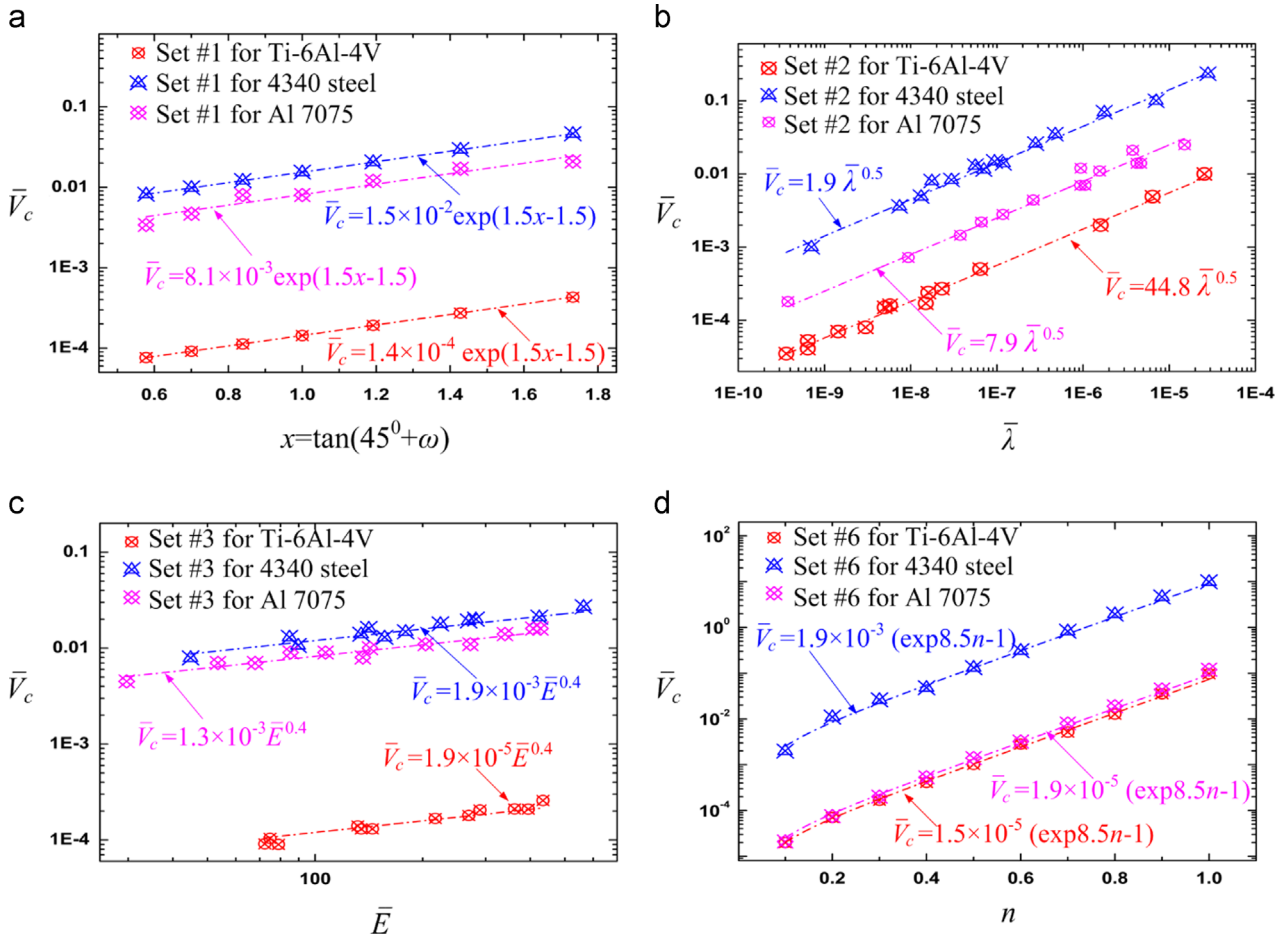

Fig. 4. $\bar{V}_c$ evolves with (a) ω, (b) $\bar{\lambda}$, (c) $\bar{E}$ and (d) n for different parameter combinations.

Table 5
The conditions for the additional simulations.

Set number	variable parameter	The combination of other dimensionless parameters										ω (deg)	Values of variables	Data number
		Material	$\bar{\lambda}\times10^{-6}$	$\bar{E}$	$\bar{A}$	$\bar{B}$	n	$C\times10^{-2}$	$\dot{\bar{\varepsilon}}_0\times10^{-12}$	$\bar{T}_m$	m			
11	$\bar{A}$	Ti–6Al–4V	5.77	152	–	–	0.28	2.8	2.5	5.27	1.0	0	A=100,200,400,600,800,1000,1200,1400 MPa, when B=100, 200, 400, 800, 1400 MPa.	8∗5=40
12	$\bar{B}$	Ti–6Al–4V	5.77	152	–	–	0.28	2.8	2.5	5.27	1.0	0	B=100,200,400,600,800,1000,1200,1400 MPa, when B=100,200,400,800,1400 MPa.	8∗5=40
13	C	Ti–6Al–4V	5.77	152	1.13	0.72	0.28	–	–	5.27	1.0	0	C=0.005, 0.01, 0.015, 0.02, 0.025, 0.03, 0.035, 0.04, 0.045, 0.05. when $\dot{\varepsilon}_0=1\times10^{-5}$, 1, 1×10^5.	10∗3=30
14	$\dot{\bar{\varepsilon}}_0$	Ti–6Al–4V	5.77	152	1.13	0.72	0.28	–	–	5.27	1.0	0	$\dot{\varepsilon}_0=1\times10^{-5}$, 1×10^{-3}, 1, 1×10^3, 1×10^5; or b=50,200,400 μm; or c=200,600,1000 J kg^{-1} K^{-1}, when C=0.005, 0.025, 0.05.	11∗3=33
15	$\bar{T}_m$	Ti–6Al–4V	5.77	152	1.13	0.72	0.28	2.8	2.5	–	–	0	T_m=700, 900, 1100, 1300, 1500, 1700, 1900, 2100, 2300 K, when m=0.50, 1.00, 1.50, 2.00.	9∗4=36
16	m	Ti–6Al–4V	5.77	152	1.13	0.72	0.28	2.8	2.5	–	–	0	m=0.50, 0.75, 1.00, 1.25, 1.50, 1.75, 2.00. when T_m=700, 1100, 1500, 1900, 2300 K.	7∗5=35

Recht's classical criterion for the onset of serrated chip flow. In Recht's model [17], it was assumed that the emergence of serrated chip flow requires a maximum in the shear stress–shear strain curve, that is

$$\frac{d\tau}{d\gamma}\le 0 \tag{10}$$

where τ and γ are the shear stress and shear strain in the PSZ, respectively.

In general, the criterion (10) can be further written as

$$Q+R\frac{d\dot{\gamma}}{d\gamma}-P\frac{dT}{d\gamma}\le 0 \tag{11}$$

where $\dot{\gamma}$ is the shear strain rate inside PSZ. Here $Q=\partial\tau/\partial\gamma$, $R=\partial\tau/\partial\dot{\gamma}$ and $P=-\partial\tau/\partial T$ reflect the effect of strain hardening, strain rate hardening and thermal softening, respectively.

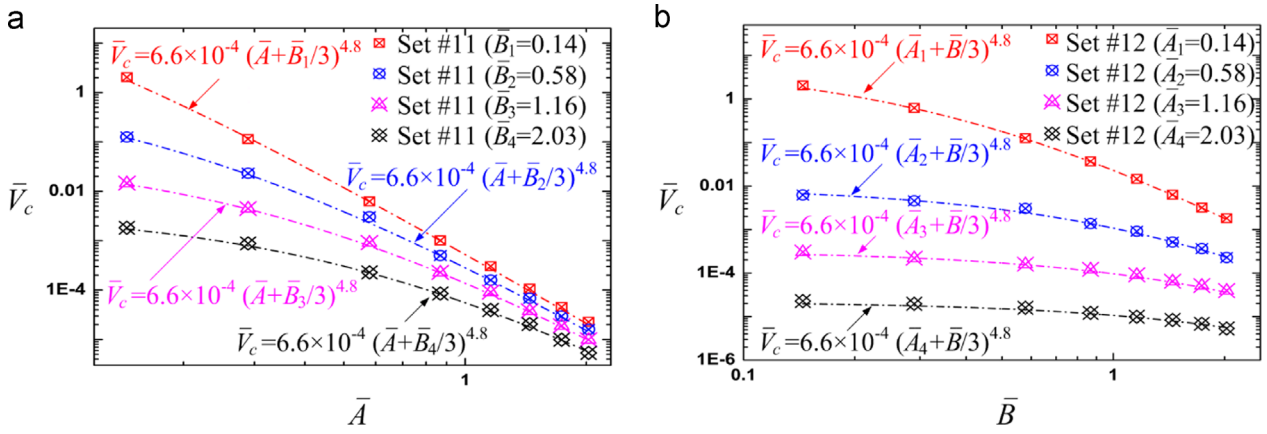

Fig. 5. (a) $\bar{V}_c$ evolves with $\bar{A}$ for different $\bar{B}$ and (b) $\bar{V}_c$ evolves with $\bar{B}$ for different $\bar{A}$.

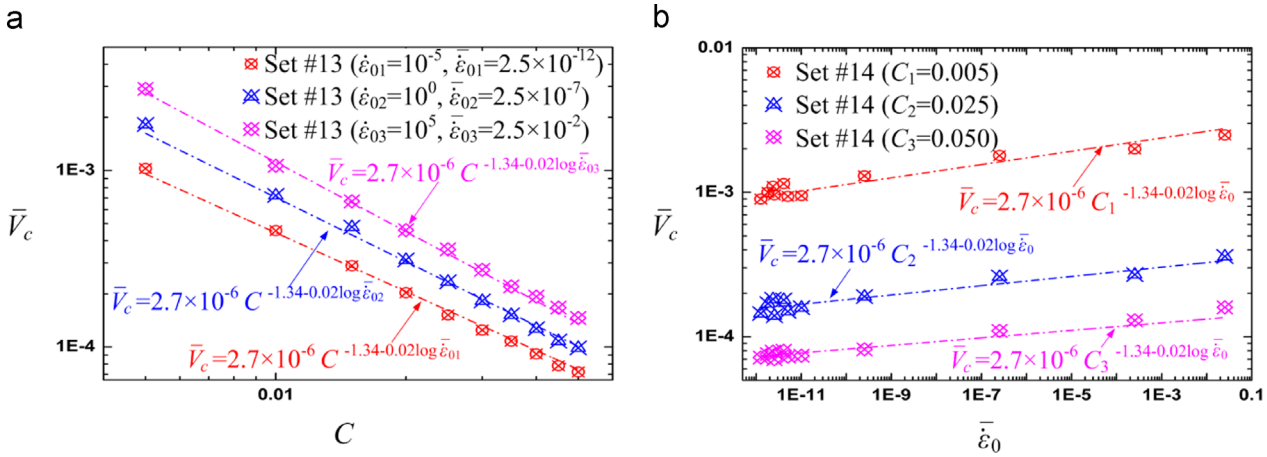

Fig. 6. (a) $\bar{V}_c$ evolves with C for different $\bar{\dot{\varepsilon}}_0$ and (b) $\bar{V}_c$ evolves with $\bar{\dot{\varepsilon}}_0$ for different C.

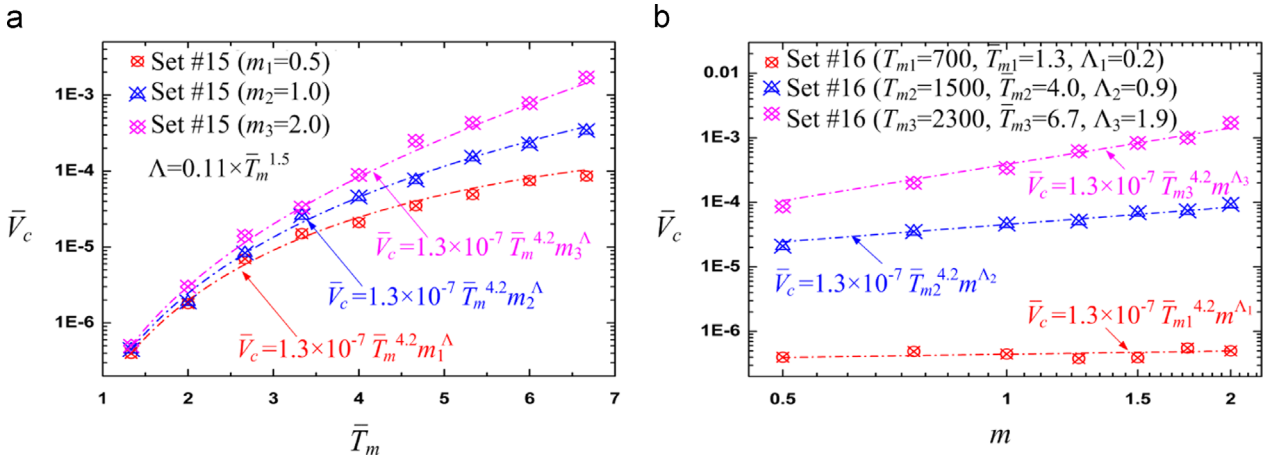

Fig. 7. (a) $\bar{V}_c$ evolves with $\bar{T}_m$ for different m and (b) $\bar{V}_c$ evolves with m for different $\bar{T}_m$.

In HSM, the plastic deformation inside PSZ is usually treated as adiabatic [71], Thus $dT/d\gamma$ in Eq. (11) can be given as

$$\frac{dT}{d\gamma}=\frac{\beta\tau}{\rho c} \tag{12}$$

Moreover, prior to the onset of serrated chip flow, the plastic deformation in PSZ is uniform, and the shear strain rate can be treated as constant, that is

$$\frac{d\dot{\gamma}}{d\gamma}=0 \tag{13}$$

Inserting Eqs. (12) and (13) into (11), and keep $Q>0$ and $P>0$ in mind, Recht's criterion can be rewritten as

$$\Pi=\frac{\beta\tau P}{\rho c Q}\geq 1 \tag{14}$$

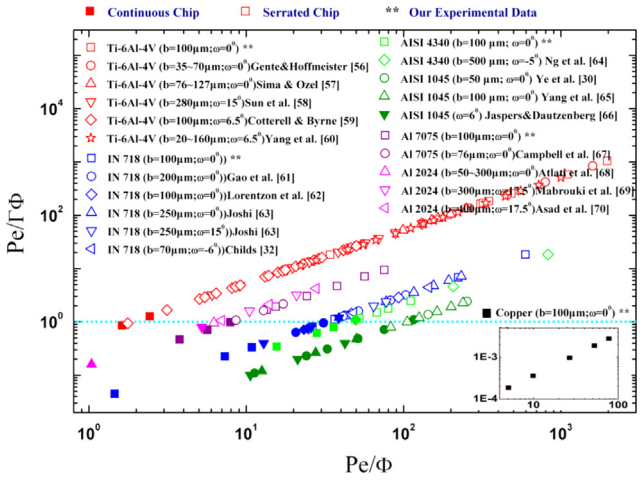

Fig. 8. Evolution of $Pe/\Gamma\Phi$ as a function of Pe/Φ for various work materials.

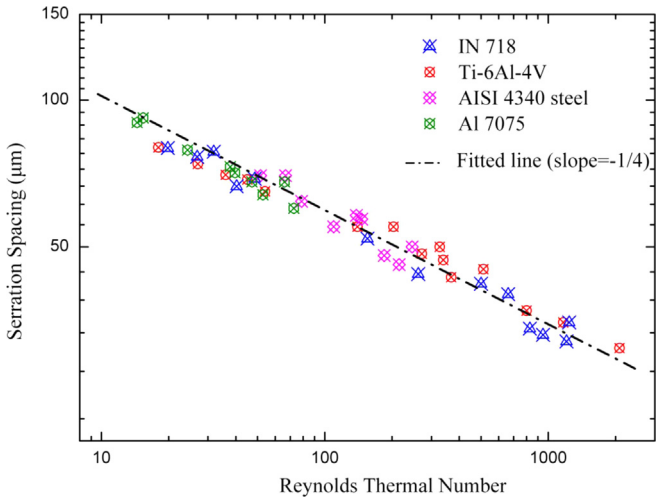

Fig. 9. Serration spacing plotted with the Reynolds thermal number ($b=100$ μm; $\omega=0°$).

This instability criterion is in accordance with the criterion proposed by Bai [72], which is derived based on the perturbation analysis to characterize the onset of thermo-plastic shear band for simple shearing. It indicates that when the tendency of the material in PSZ to harden with plastic deformation is overtaken by thermal softening effects, thermo-plastic shear instability occurs, and the serrated chip flow forms.

The instability criterion (14) shows clearly that increase in shear stress τ and thermal softening effect P accelerate the instability, whereas increasing the strain hardening effect Q retards the onset of serrated chip flow.

It should be pointed out that, the HSM process is much more complex than simple shearing, and the temperature rise inside PSZ could be affected by thermal diffusion and material convection that are caused by the rapid chip flow in HSM [26,30]. So, the instability criterion (14), which is obtained based on the adiabatic assumption, cannot be strictly applied to predict the critical condition for the onset of serrated chip flow. However, it gives clues to investigate the influences of material parameters on the chip flow instability.

5.2. The influence of the initial yield stress A and hardening modulus B

The critical Reynolds thermal number Pe_c plotted with $\overline{A}$ for various $\overline{B}$ is shown in Fig. 10a. There exists a scaling low between Pe_c and $(\overline{A}+\overline{B}/3)$ as

$$Pe_c \propto (\overline{A}+\overline{B}/3)^{-4.8} \tag{15}$$

It can be found that a higher initial yield stress A or hardening modulus B leads to a lower critical cutting speed at which the chip flow changes from continuous to serrated. So, increasing the initial yield stress A or hardening modulus B promotes the onset of serrated chip flow.

A higher initial yield stress usually indicates a higher hardness [73]. And the serrated chip flow is usually favored by increasing the material hardness [74]. Thus the serrated chip flow could be facilitated by increasing the material initial yield stress A.

For orthogonal cutting, the plane strain state is adopted, thus the J-C law can be given in the form of shear stress as

$$\tau=\frac{1}{\sqrt{3}}\left(A+B\left(\frac{\gamma}{\sqrt{3}}\right)^{n}\right)\left[1+C\ln\left(\frac{\dot{\gamma}}{\sqrt{3}\dot{\varepsilon}_0}\right)\right]\left[1-\left(\frac{T-T_0}{T_m-T_0}\right)^{m}\right] \tag{16}$$

The J–C law (16) indicates that a higher initial yield stress A results in a higher shear stress τ, leading to a higher energy consuming and hence a higher temperature rise (see Eq. (12)) (the average shear strain inside PSZ can be regarded as constant before instability occurs). This facilitates the shear banding and hence promotes the emergence of serrated chip flow. Form Recht's instability criterion (14) it also can be found that a higher shear stress τ renders a higher Π and thus promotes the instability. This is in accordance with the tendency described by Eq. (15).

On the other hand, a higher hardening modulus B indicates a higher strain hardening, which seems to have a negative effect on the instability initiation. However, it should be noticed that a higher B also means a higher flow stress, which facilitates the serrated chip flow. Inserting the J–C law into Recht's instability criterion (14) we can get that

$$\Pi \propto \frac{(A+B(\gamma/\sqrt{3})^{n})^2}{B} \tag{17}$$

This shows clearly that increasing the hardening modulus B also accelerates the flow instability and thus promotes the onset of serrated chip flow. Eq. (17) also implies that, increasing the initial yield stress promotes the instability much more obviously than increasing the hardening modulus. This shows a similar tendency with Eq. (15), in which the hardening modulus is multiplied by a smaller coefficient (1/3) while the initial yield stress is multiplied by a bigger one (1).

5.3. The influence of the hardening exponent n

The evolution of Pe_c as a function of n is plotted in Fig. 10b. The critical Reynolds thermal number Pe_c is linearly proportional to $e^{8.5n}-1$. It is shown that increasing the hardening exponent n hinders the emergence of serrated chip flow.

A larger hardening exponent n usually implies a stronger effect of strain hardening, which retards the shear banding and thus hinders the onset of serrated chip flow. Indeed, for the J–C law the strain hardening effect Q dependents on the strain hardening exponent n as $Q \propto n(\gamma/\sqrt{3})^{n-1}$. According to Oxley [75], the average shear strain inside the primary shear zone can be estimated as

$$\gamma = \cos\omega/2\ \sin\varphi\ \cos(\varphi-\omega) \tag{18}$$

where the shear angle can be given by $\varphi=\pi/4-(\arctan\mu)/2+\omega/2$ [76].

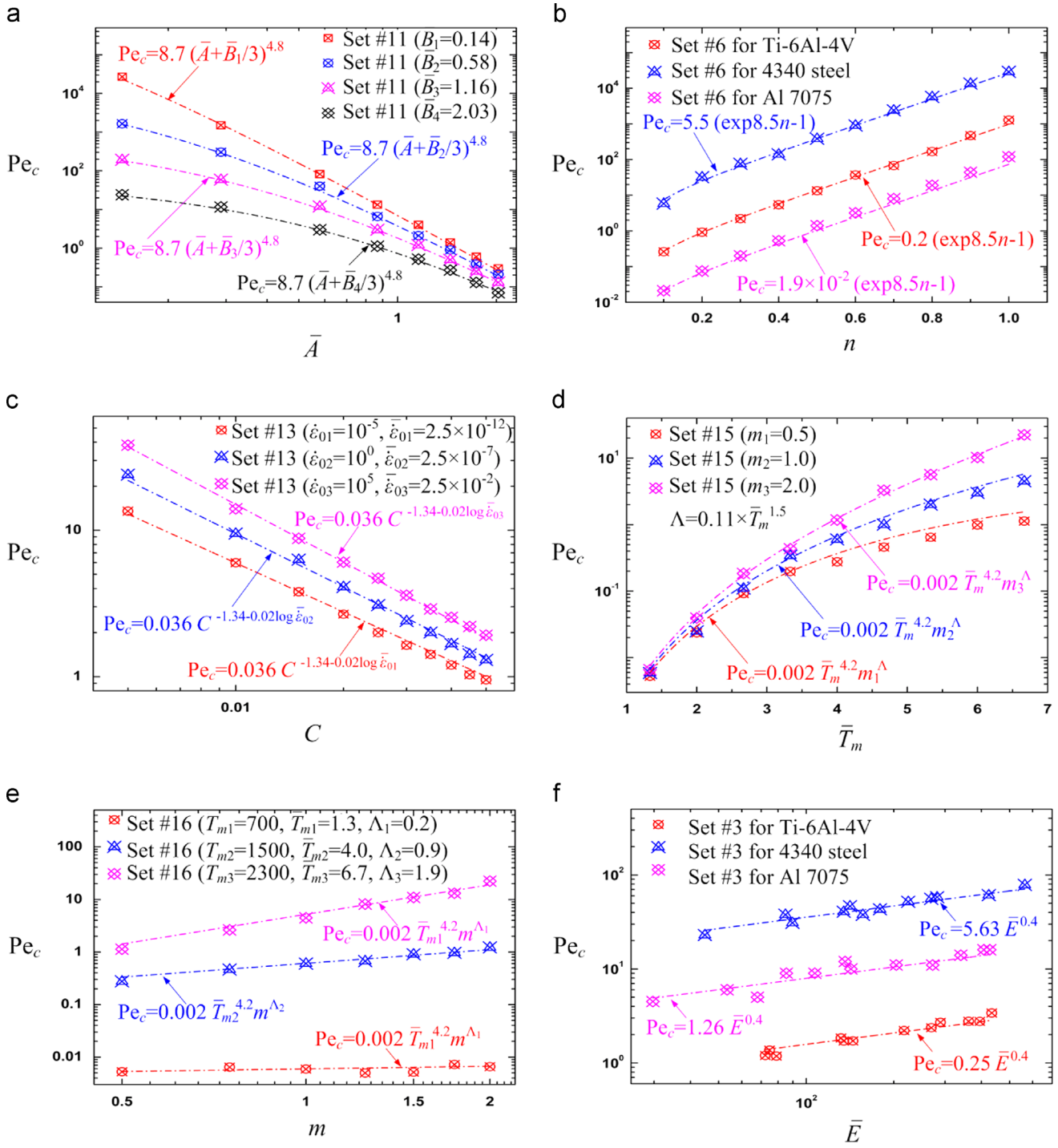

Fig. 10. Evolutions of Pe_c as functions of (a) $\bar{A}$, (b) n, (c) C, (d) $\bar{T}_m$, (e) m and (f) $\bar{E}$. The constant coefficients of the fitted lines are in agrees with the values calculated from Eq. (7).

Thus the average shear strain γ is usually in the range of 0.7–1.5 ($-15^\circ \le \omega \le 15^\circ$; $0 \le \mu \le 0.3$). So, in the investigated range of $0.1 \le n \le 1$, the strain hardening effect Q always increases with increasing the hardening coefficient n (see Fig. 11). This retards the thermo-plastic shear instability (see Eq. (14)), and thus hinders the onset of serrated chip flow.

Moreover, to quantitatively compare the present model with Recht's classical model, Fig. 12 gives the evolutions of $Pe/\Gamma\Phi$ and Π as functions of n for AISI 4340 steel (V=10 m/s, b=100 μm, ω=0°). Here, to work out the value of Π, the shear strain γ was estimated by Eq. (18), and the temperature rise ΔT and shear strain rate $\dot{\gamma}$ were approximately estimated as [26,75]

$$\Delta T = \frac{\beta\tau\gamma}{\rho c} \tag{19}$$

$$\dot{\gamma} = 10V\ \cos\ \omega / b\ \cos(\varphi - \omega) \tag{20}$$

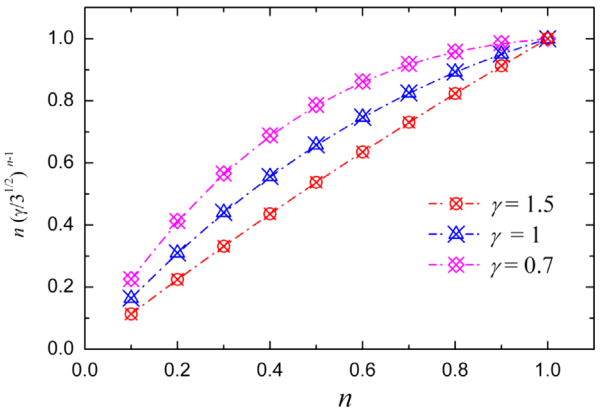

Fig. 11. Evolution of $n(\gamma/\sqrt{3})^{n-1}$ as a function of n.

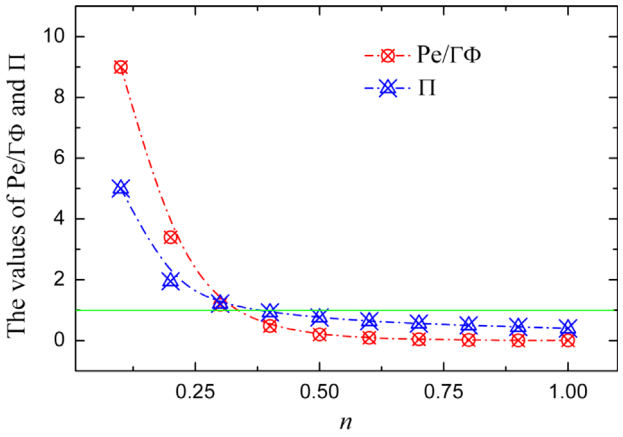

Fig. 12. Evolutions of $\mathrm{Pe}/\Gamma\Phi$ and Π as functions of n for AISI 4340 steel ($V=10$ m/s, $b=100$ μm, $\omega=0^\circ$).

It can be found from Fig. 12 that, the present model has a same varying tendency with Recht's classical model: when $\mathrm{Pe}/\Gamma\Phi$ and Π are larger than one, both of them decrease rapidly with increasing n; and when $\mathrm{Pe}/\Gamma\Phi$ and Π become smaller than one, both of them decrease much more slowly with increasing n. More importantly, $\mathrm{Pe}/\Gamma\Phi=1$ and $\Pi=1$ take place almost at a same n, which indicates that the critical condition for the onset of serrated chip flow predicted by the present model is in accordance with that predicted by Recht's classical model.

5.4. The influence of the strain rate dependency coefficient C

Fig. 10c shows the evolution of Pe_c with C for various values of $\dot{\bar{\varepsilon}}_0$. The critical Reynolds thermal number for the onset of serrated chip flow follows a power low dependence on the strain rate coefficient C as $\mathrm{Pe}_c \propto C^{-1.34-0.02\log\dot{\bar{\varepsilon}}_0}$. It can be found that increasing the strain rate dependency coefficient C facilitates the emergence of serrated chip flow.

A higher C indicates a higher flow stress τ due to strain rate hardening. This leads to a higher temperature rise (see Eq. (19)) and thus accelerates the onset of serrated chip flow. Taking the J–C law into Recht's instability criterion (14) we can get that the dimensionless number Π is approximately proportional to $1+C\ln(\dot{\gamma}/\sqrt{3}\dot{\varepsilon}_0)$. Therefore, the instability criterion can be satisfied much more easily for a higher C, which is positive for the emergence of serrated chip flow. Moreover, increasing the reference strain rate $\dot{\varepsilon}_0$ leads to a lower Π and thus hinders the onset of serrated chip flow. This is in accordance with that implied in Fig. 10c, in which a higher reference strain rate leads to a higher critical cutting speed.

5.5. The influence of the melting temperature T_m and initial temperature T_0

Fig. 10d gives the variation of Pe_c with respect to $\overline{T}_m$. It shows that the critical Reynolds thermal number Pe_c depends linearly on $\overline{T}_m^{4.2}$. Indeed, from Eq. (7) it can be found that the critical cutting speed for the onset of serrated chip flow is approximately dependent on the melting and initial temperatures as $V_c \propto (T_m-T_0)^{4.2}$. Thus increasing the melting temperature T_m or reducing the initial temperature T_0 hinders the onset of serrated chip flow.

Higher T_m or lower T_0 means the work material can be softened by heating due to plastic deformation much harder. This retards the shear band initiation and hence hinders the emergence of serrated chip flow. It should be noticed that, the thermal softening effect P in the instability criterion (14) is approximately proportional to $(T_m-T_0)^{-m}$. Noticing that the thermal softening coefficient m is positive. So, increasing the melting temperature or reducing the initial temperature could weaken the thermal softening effect and thus stabilizes the thermo-plastic shear deformation.

5.6. The influence of the thermal softening coefficient m

The evolution of the critical Reynolds thermal number as a function of the thermal softening coefficient m is shown in Fig. 10e. The critical Reynolds thermal number Pe_c varies with m according to $\mathrm{Pe}_c \propto m^{\Lambda}$, where $\Lambda = 6(\rho c\overline{T}_m T_0/10^{10}\ \mathrm{J})^{1.5}$. Increasing the thermal softening coefficient m has a stabilizing effect on the thermo-plastic shear deformation which hinders the onset of serrated chip flow.

Similar to the effect of melting temperature T_m, the work material is much harder to be softened by heating due to plastic deformation for a larger m. For the J–C law, the thermal softening effect P is approximately proportional to m as

$$P \propto m(\Delta T/T_m^*)^{m-1} \tag{21}$$

The temperature rise in the PSZ prior to shear banding can be roughly estimated from Eq. (19). And thus the temperature rise for the applied work materials (copper, Al 7075, AISI 4340 steel, Ti–6Al–4V and IN 718) can be worked out, as shown in Table 6 ($0.7<\gamma<1.5$). It can be noticed that the nickel-base superalloy IN 718 has a maximum temperature rise (295 K) at $\gamma_{max}=1.5$, while the copper has a minimum one (11 K) at $\gamma_{min}=0.7$. And $\Delta T/T_m^*$ has a maximum value about 0.3 at $\gamma_{max}=1.5$ for the aluminum alloy Al 7075. It should be pointed out that, in the range of $0<\Delta T/T_m^*<0.3$, the term $m(\Delta T/T_m^*)^{m-1}$ decreases with increasing m, as shown in Fig. 13. Thus, increasing the thermal softening coefficient m could weaken the thermal softening effect, which stabilize the thermo-plastic shear deformation and hinders the onset of serrated chip flow. This trend is in accordance with that implied in Fig. 10e.

Moreover, Fig. 14 gives the evolutions of $\mathrm{Pe}/\Gamma\Phi$ and Π as functions of m for AISI 4340 steel ($V=10$ m/s, $b=100$ μm, $\omega=0^\circ$). It is found that, $\mathrm{Pe}/\Gamma\Phi$ and Π have same tendency with changing the thermal softening coefficient m, and the $\mathrm{Pe}/\Gamma\Phi=1$ and $\Pi=1$ almost take place at a same m. This shows clearly that the present model has a same varying tendency with Recht's classical model.

Table 6
Temperature rise in the PSZ before shear banding.

	Copper	Al 7075	AISI 4340	Ti–6Al–4V	IN 718
ΔT (K) (γ=0.7)	11	81	77	124	138
ΔT (K) (γ=1.5)	23	174	166	265	295
$\Delta T/T_m^*$ (γ=0.7)	0.010	0.137	0.052	0.078	0.108
$\Delta T/T_m^*$ (γ=1.5)	0.022	0.293	0.111	0.168	0.232

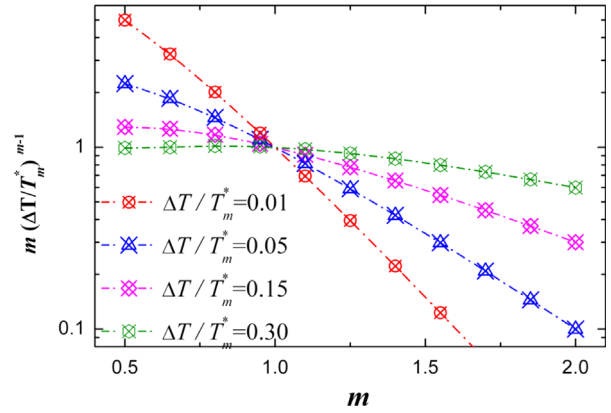

Fig. 13. Evolution of $m(\Delta T/T_m^*)^{m-1}$ as a function of m.

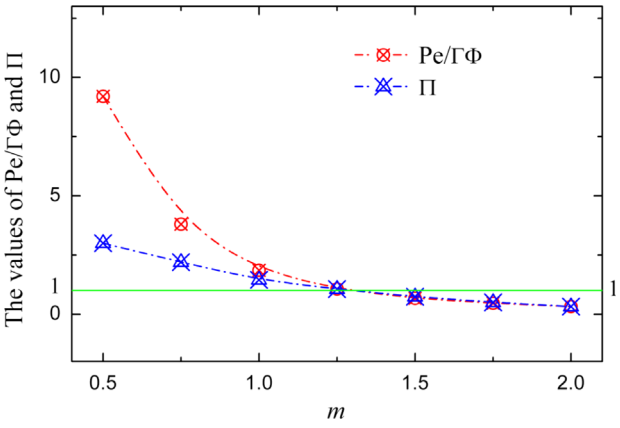

Fig. 14. Evolutions of Pe/$\Gamma\Phi$ and Π as functions of m for AISI 4340 steel (V=10 m/s, b=100 μm, ω=0°).

5.7. The influence of the elastic modulus E

The evolution of Pe_c as a function of $\overline{E}$ is shown in Fig. 10f. The critical Reynolds thermal number follows a power low dependent on the elastic modulus as $Pe_c \propto \overline{E}^{0.4}$. It shows that increasing the elastic modulus has a negative effect on the onset of serrated chip flow.

A higher E means more energy could be stored in elastic deformation while less energy could be divided to heating the work material through plastic flow. This retards the thermal softening and thus hinders the emergence of serrated chip flow.

Moreover, during cutting, the tool exerts a force on the chip over their contact surface, making the chip deform in a local compressive deformation zone. The tool–chip compressive stress induces a gradient in the shear stress, leading to the large scale shearing deformation that takes place in the PSZ. Thus the thermo-plastic shear deformation and the energy input into the PSZ are dominated by the tool–chip compression. It should be noticed that, the elastic unloading of the tool–chip compression could take place as the compressive stress reaches its yield limit [32]. Therefore, increasing the elastic modulus E promotes the elastic unloading of the tool–chip compression, leading to a reduction of the energy input into the PSZ and thus retards the onset of serrated chip flow.

5.8. The influence of the heat generation term ρc

According to Eq. (7), the critical cutting speed for the onset of serrated chip flow depends on the material density and specific heat as $V_c \propto (\rho c)^{3.4}$. It shows that increasing the heat generation term ρc hinders the onset of serrated chip flow.

The heat generation term ρc describes the energy consuming for unit temperature rise. According to (19), increasing ρc leads to a diminution of the temperature rise for a given value of shear strain. As a consequence, the stress drop due to thermal softening is weaker, which has a stabilized effect on the thermo-plastic shear deformation inside the PSZ. Indeed, from the instability criterion (14) it also can be easily found that, higher ρc retards the thermo-plastic shear instability and hence hinders the onset of serrated chip flow.

6. Conclusions

HSM experiments of IN 718, Ti–6Al–4V, AISI 4340 steel, Al 7075 and copper was undertaken with cutting speed ranging from 0.05 to 90 m/s. The microscopic observations of chips reveal that the transition from continuous chip flow to serrated chip flow can be attributed to a repeated shear band formation inside PSZ, and the onset of serrated chip flow has a strong dependence on the work material. The dimensionless analysis and finite element simulations were carried out to obtain the critical cutting speed at which the serrated chip flow is produced. The universal expression of the critical cutting speed for cutting metallic materials by using sharp tools is achieved. It is given in terms of material properties, uncut chip thickness and tool rake angle. The predictions of the critical cutting speeds show good agreements with the experimental findings for various metal materials over wide ranges of uncut chip thickness and tool rake angle. Moreover, it is found that there exist striking similarity between the serrated chip flow and the turbulent fluid flow. As the laminar–turbulent transition of the fluid is dominated by the Reynolds number, the continuous–serrated transition of the chip flow is controlled by a Reynolds thermal number. And this Reynolds thermal number also controls the evolution of the serrated chip flow as the serration spacing is followed a power law dependence on the Reynolds thermal number. At last, the influences of the material properties on the onset of serrated chip flow are systematically investigated. It shows that increasing the work material density, specific heat, thermal conductivity, elastic modulus, melting temperature, reference strain rate, work-hardening exponent and the thermal softening coefficient hinders the onset of serrated chip flow, while increasing the material initial yield stress, hardening modulus, strain rate dependency coefficient and the reference temperature promotes the emergence of serrated chip flow. This shows good agreement with Recht's classical criterion.

Acknowledgment

This work was supported by the Nature Science Foundation of China (Grants nos. 11132011 and 11202221), the National Basic

Research Program of China (Grant no. 2012CB937500) and the China Postdoctoral Science Foundation (Grant no. 2013M540148).

Appendix A. Numerical simulation

A.1. Modeling

Based on the experimental findings, the finite element simulations were applied to capture the critical cutting speed at which the chip flow transition from continuous to serrated takes place.

A plane strain model of orthogonal cutting is developed using the finite element code ABAQUS/Explicit with Lagrangian formulation. The basic geometry of the numerical model is presented in Fig. A1. The work material is fixed at the lowest contour and the cutting speed is applied to the tool. The tool is treated here for simplicity as an analytical rigid body.

The mesh of the work material is divided into three parts: the uncut chip material (zone A), the fracture material (zone B) and the leaving material (zone C). The upper boundary of zone C corresponds to the machined surface. The meshes in zones B and C are parallel to horizontal and vertical directions, while the meshes in the zone A are characterized by an inclination angle δ with the tool surface. An optimal orientation $\delta=45^{\circ}$ is adopted here to facilitate the formation of segmented chip flow [77].

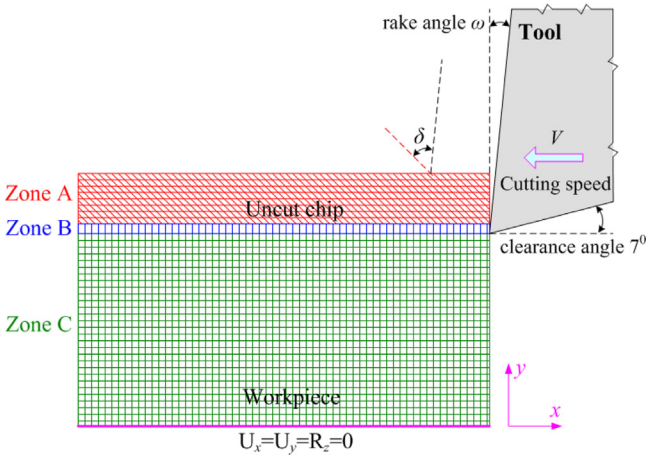

Fig. A1. The schematic diagram of numerical model.

A fully coupled thermal–mechanical analysis is carried out by considering CPE4RT elements, which are plane strain, quadrilateral, linearly interpolated, and thermally coupled elements with reduced integration and automatic hourglass control. The work material is taken as elastic–viscoplastic. And the plastic flow is governed by the J-C law.

The extended Coulomb friction model is chosen in this work to model the tool–chip interaction, and the friction coefficient is set to be 0.3 as a constant.

The separation of the chip from the workpiece is modeled with the help of a failure zone, see the zone B in Fig. A1. Up to failure, this zone behaves according to the J–C model. The failure of this zone takes place at a critical value γ_p of the accumulated equivalent inelastic deformation, and hence the chip separates from the surrounding workpiece in a defined distance from the tool tip. In this work, the γ_p is set to a value of 2.0 [78].

A.2. Validation of the finite element model

To validate the numerical model developed above, the finite element simulations of high speed cutting of Ti–6Al–4V from 0.05 m/s to 35 m/s were carried out. The uncut chip thickness and tool rake angle were set as 100 μm and 0°, respecctively. The serrated chip morphology can be characterized by three parameters, i.e., serration spacing, valley and peak (see Fig. A2a). The comparison of the simulated and experimental chip morphology is presented in Fig. A2b. It can be seen that the simulated chip morphologies agree well with the experimental ones. The good agreements between the simulated and experimental results indicates that the finite element simulations employed in this work can give accurate predictions for the chip mophologies.

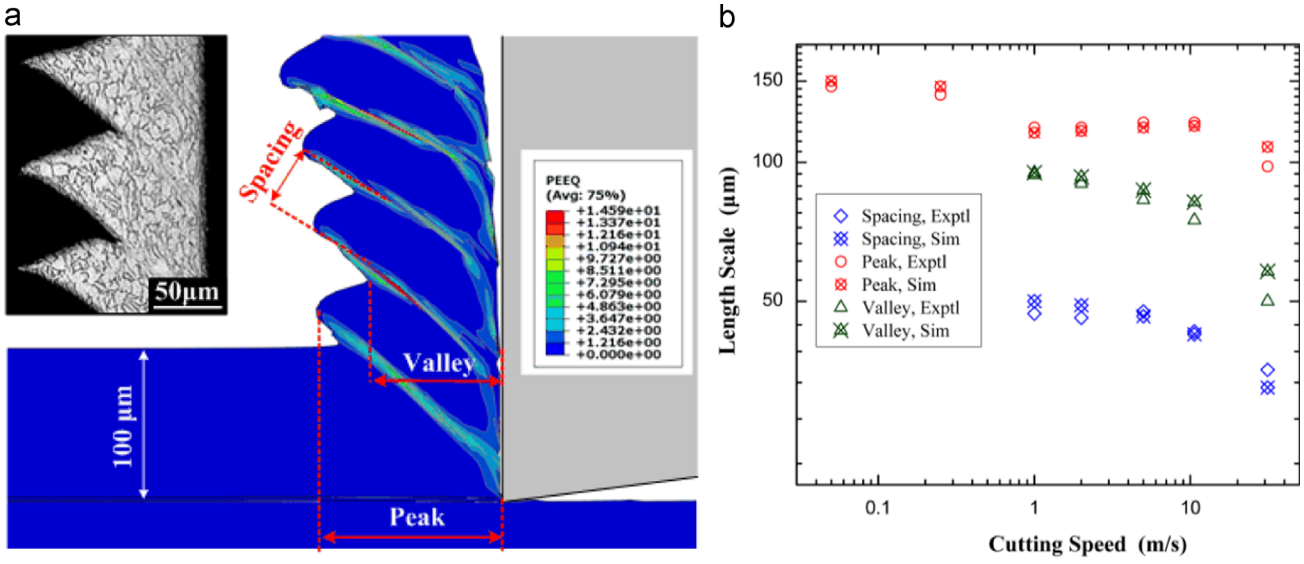

Fig. A2. (a) Simulated chip morphology for Ti–6Al–4V at $V=5$ m/s and (b) comparison of simulated chip dimensions with experimental data.

References

[1] M.C. Shaw, Metal Cutting Principles, 2nd ed., Oxford University Press, New York, 2005.
[2] A.G. Atkins, The Science and Engineering of Cutting, Elsevier, Oxford, 2009.
[3] B. Wang, Z.Q. Liu, Q.B. Yang, Investigations of yield stress, fracture toughness, and energy distribution in high speed orthogonal cutting, Int. J. Mach. Tools Manuf. 73 (2013) 1–8.
[4] R.S. Pawade, S.S. Joshi, P.K. Brahmankar, Effect of cutting edge geometry and machining parameters on surface integrity of high-speed turned Inconel 718, Int. J. Mach. Tools Manuf. 48 (2008) 15–28.
[5] G. Sutter, G. List, Very high speed cutting of Ti–6Al–4V titanium alloy – change in morphology and mechanism of chip formation, Int. J. Mach. Tools Manuf. 66 (2013) 37–43.
[6] M.A. Davies, Y. Chou, C.J. Evans, On chip morphology, tool wear and cutting mechanics in finish hard turning, CIRP Ann. 45 (1996) 77–82.
[7] M.C. Shaw, A. Vyas, Chip formation in the machining of hardened steel, CIRP Ann. 42 (1993) 29–33.
[8] J. Barry, G. Byrne, D. Lennon, Observations on chip formation and acoustic emission in machining Ti–6Al–4V alloy, Int. J. Mach. Tools Manuf. 41 (2001) 1055–1070.
[9] C.Z. Duan, L.C. Zhang, Adiabatic shear banding in AISI 1045 steel during high speed machining: mechanisms of microstructural evolution, Mater. Sci. Eng. A 532 (2012) 111–119.
[10] H. Wang, S. To, C.Y. Chan, C.F. Cheung, W.B. Lee, Elastic strain induced shear bands in the microcutting process, Int. J. Mach. Tools Manuf. 50 (2010) 9–18.
[11] H. Wang, S. To, C.Y. Chan, C.F. Cheung, W.B. Lee, A study of regularly spaced shear bands and morphology of serrated chip formation in microcutting process, Scr. Mater. 63 (2010) 227–230.
[12] H. Wang, S. To, C.Y. Chan, C.F. Cheung, W.B. Lee, Dynamic modelling of shear band formation and tool-tip vibration in ultra-precision diamond turning, Int. J. Mach. Tools Manuf. 51 (2011) 512–519.
[13] B. Dodd, Y.L. Bai, Adiabatic Shear Localization, 2nd ed., Elsevier, London, 2012.
[14] S.P. Joshi, K.T. Ramesh, Rotational diffusion and grain size dependent shear instability in nanostructured materials, Acta Mater. 56 (2008) 282–291.
[15] S.P. Joshi, K.T. Ramesh, Stability map for nanocrystalline and amorphous materials, Phys. Rev. Lett. 101 (2008) 025501.
[16] T.W. Wright, H. Ockendon, A scaling law for the effect of inertia on the formation of adiabatic shear bands, Int. J. Plast. 12 (1996) 927–934.
[17] R.F. Recht, Catastrophic thermoplastic shear, J. Appl. Mech. 31 (1964) 189–193.
[18] B.F. von-Turkovich, D.R. Durham, Machining titanium and its alloys, in: Advanced Processing Methods for Titanium, Metallurgical Society of AIME Conference, 1982, pp. 257–274.
[19] Z.B. Hou, R. Komanduri, Modeling of thermomechanical shear instability in machining, Int. J. Mech. Sci. 39 (1997) 1279–1314.
[20] R. Komanduri, Z.B. Hou, On thermoplastic shear instability in the machining of a titanium alloy (Ti–6Al–4V), Metall. Trans. A 33A (2002) 2995–3010.
[21] S.L. Semiatin, S.B. Rao, Shear localization during metal cutting, Mater. Sci. Eng. A 61 (1983) 185–192.
[22] J.Q. Xie, A.E. Bayoumi, H.M. Zbib, Analytical and experimental study of shear localization in chip formation in orthogonal machining, J. Mater. Eng. Perform. 4 (1995) 32–39.
[23] J.Q. Xie, A.E. Bayoumi, H.M. Zbib, A study on shear banding in chip formation of orthogonal machining, Int. J. Mach. Tools Manuf. 36 (1996) 835–847.
[24] A. Molinari, D. Dudzinski, Stationary shear band in high-speed machining, C. R. Acad. Sci. Paris 315 (1992) 399–405.
[25] T.J. Burns, M.A. Davies, Nonlinear dynamics model for chip segmentation in machining, Phys. Rev. Lett. 79 (1997) 447–450.
[26] T.J. Burns, M.A. Davies, On repeated adiabatic shear band formation during high-speed machining, Int. J. Plast. 18 (2002) 487–506.
[27] J. Huang, E.C. Aifantis, A note on the problem of shear localization during chip formation in orthogonal machining, J. Mater. Eng. Perform. 6 (1997) 25–26.
[28] J. Huang, K. Kalaitzidou, J.W. Sutherland, E.C. Aifantis, Validation of a predictive model for adiabatic shear band formation in chips produced via orthogonal machining, J. Mech. Behav. Mater. 18 (2007) 243–263.
[29] G.H. Li, M.J. Wang, C.Z. Duan, Adiabatic shear critical condition in the high-speed cutting, J. Mater. Process. Technol. 209 (2009) 1362–1367.
[30] G.G. Ye, S.F. Xue, W. Ma, M.Q. Jiang, Z. Ling, X.H. Tong, L.H. Dai, Cutting AISI 1045 steel at very high speeds, Int. J. Mach. Tools Manuf. 56 (2012) 1–9.
[31] W. Ma, X.W. Li, L.H. Dai, Z. Ling, Instability criterion of materials in combined stress states and its application to orthogonal cutting process, Int. J. Plast. 30–31 (2012) 18–40.
[32] T.H.C. Childs, Adiabatic shearing in metal machining, in: L. Laperrière, G. Reinhart (Eds.), CIRP Encyclopedia of Production Engineering, Springer, Berlin, 2013.
[33] M. Bäker, J. Rösler, C. Siemers, A finite element model of high speed metal cutting with adiabatic shearing, Comput. Struct. 80 (2002) 495–513.
[34] M. Bäker, Finite element investigation of the flow stress dependence of chip formation, J. Mater. Process. Technol. 167 (2005) 1–13.
[35] S. Rhim, S. Oh, Prediction of serrated chip formation in metal cutting process with new flow stress model for AISI 1045 steel, J. Mater. Process. Technol. 171 (2006) 417–422.
[36] P.J. Arrazola, A Villar, D. Ugarte, S. Marya, Serrated chip prediction in finite element modeling of the chip formation process, Mach. Sci. Technol. 11 (2007) 367–390.
[37] P.J. Arrazola, O Barbero1, I. Urresti, Influence of material parameters on serrated chip prediction in finite element modeling of chip formation process, Int. J. Mater. Form. 3 (2010) 519–522.
[38] M. Issa, C. Labergère, K. Saanouni, A. Rassineux, Numerical prediction of thermomechanical field localization in orthogonal cutting, J. Manuf. Sci. Technol. 5 (2012) 175–195.
[39] C.Z. Duan, L.C. Zhang, A reliable method for predicting serrated chip formation in high-speed cutting: analysis and experimental verification, Int. J. Adv. Manuf. Technol. 64 (2013) 1587–1597.
[40] C.Y. Gao, L.C. Zhang, Effect of cutting conditions on the serrated chip formation in high-speed cutting, Mach. Sci. Technol. 17 (2013) 26–40.
[41] M.H. Miguélez, X. Soldani, A. Molinari, Analysis of adiabatic shear banding in orthogonal cutting of Ti alloy, Int. J. Mech. Sci. 75 (2013) 212–222.
[42] A.E. Bayoumi, J.Q. Xie, Some metallurgical aspects of chip formation in cutting Ti–6 wt%Al–4 wt%V alloy, Mater. Sci. Eng. A 190 (1995) 173–180.
[43] K.M. Cho, Y.C. Chi, J. Duffy, Microscopic observations of adiabatic shear bands in three different steels, Metall. Trans. A 21 (1990) 1161–1175.
[44] G. Hussain, A. Hameed, J.G. Hetherington, P.C. Barton, A.Q. Malik, Hydrocode simulation with modified Johnson–Cook model and experimental analysis of explosively formed projectiles, J. Energy Mater. 31 (2013) 143–155.
[45] N.S. Brar, V.S. Joshi, B.W. Harris, Constitutive model constants for Al 7075-T651 and Al7075-T6, in: M.L. Elert, W.T. Buttler, M.D. Furnish, W.W. Anderson, W.G. Proud (Eds.), AIP Conference Proceedings, vol. 1195, American Institute of Physics, Nashville, 2009, pp. 945–994.
[46] G. Fang, P. Zeng, Fem investigation for orthogonal cutting process with grooved tools—technical communication, Mach. Sci. Technol. 11 (2007) 561–572.
[47] W.S. Lee, C.F. Lin, High-temperature deformation behaviour of Ti6Al4V alloy evaluated by high strain-rate compression tests, J. Mater. Process. Technol. 75 (1998) 127–136.
[48] J.M. Pereira, B.A. Lerch, Effects of heat treatment on the ballistic impact properties of Inconel 718 for jet engine fan containment applications, Int. J. Impact Eng. 25 (2001) 715–733.
[49] L.H. Lang, A.J. Xu, F. Li, Precision forging technological optimization for 7075 aluminum alloy complex component with limbs, JOM 64 (2012) 309–315.
[50] R.C. Batra, L. Chen, Shear band spacing in gradient-dependent thermovisco-plastic materials, Comput. Mech. 23 (1999) 8–19.
[51] G.G. Ye, S.F. Xue, M.Q. Jiang, X.H. Tong, L.H. Dai, Modeling periodic adiabatic shear band evolution during high speed machining Ti–6Al–4V alloy, Int. J. Plast. 40 (2013) 39–55.
[52] F.F.P. Bisacre, G.H. Bisacre, The life of carbide-tipped turning tools, Pro. Int. Mech. Eng. 157 (1947) 452–469.
[53] D.C. Drucker, H. Ekstein, A dimension analysis of metal cutting, J. Appl. Phys. 21 (1950) 104–107.
[54] N.N. Zorev, Inter-relationship between shear processes occurring along tool face and shear plane in metal cutting, International Research in Production Engineering, ASME, New York (1963) 42–49.
[55] T. Özel, T. Altan, Determination of workpiece flow stress and friction at the chip–tool contact for high-speed cutting, Int. J. Mach. Tools Manuf. 40 (2000) 133–152.
[56] A. Gente, H.W. Hoffmeister, Chip formation in machining Ti6A14V at extremely high cutting speeds, CIRP Ann. 50 (2001) 49–52.
[57] M. Sima, T. Özel, Modified material constitutive models for serrated chip formation simulations and experimental validation in machining of titanium alloy Ti–6Al–4V, Int. J. Mach. Tools Manuf. 50 (2010) 943–960.
[58] S. Sun, M. Brandt, M.S. Dargusch, Characteristics of cutting forces and chip formation in machining of titanium alloys, Int. J. Mach. Tools Manuf. 49 (2009) 561–568.
[59] M. Cotterell, G. Byrne, Dynamics of chip formation during orthogonal cutting of titanium alloy Ti–6Al–4V, CIRP Ann. 57 (2008) 93–96.
[60] Q. Yang, Z. Liu, Z. Shi, B. Wang, Analytical modelling of adiabatic shear band spacing for serrated chip in high-speed machining, Int. J. Adv. Manuf. Technol. 71 (2014) 1901–1908.
[61] D. Gao, Z.P. Hao, R.D. Han, Y.L. Chang, J.N. Muguthu, Study of cutting deformation in machining nickel-based alloy Inconel 718, Int. J. Mach. Tool. Manuf. 51 (2011) 520–527.
[62] J. Lorentzon, N. Järvstråt, B.L. Josefson, Modelling chip formation of alloy 718, J. Mater. Process. Techol. 209 (2009) 4645–4653.
[63] D. Joshi, Finite Element Simulation of Machining a Nickel-Based Superalloy – Inconel 718 (MSc thesis), University of Pune, India, 2000.
[64] E.G. Ng, T.I. El-Wardany, M. Dumitrescu, M.A. Elbestawi, Physics-based simulation of high speed machining, Mach. Sci. Technol. 6 (2002) 301–329.
[65] Q.B. Yang, Z.Q. Liu, B. Wang, Characterization of chip formation during machining 1045 steel, Int. J. Adv. Manuf. Technol. 63 (2012) 881–886.
[66] S.P.F.C. Jaspers, J.H. Dautzenberg, Material behaviour in metal cutting: strain, strain rate and temperature in chip formation, J. Mater. Process. Technol. 121 (2002) 123–135.
[67] C.E. Campbell, L.A. Bendersky, W.J. Boettinger, R. Ivester, Microstructural characterization of Al-7075-T651 chips and work pieces produced by high-speed machining, Mater. Sci. Eng. A 430 (2006) 15–26.
[68] S. Atlati, B. Haddag, M. Nouari, M. Zenasni, Analysis of a new segmentation intensity ratio SIR to characterize the chip segmentation process in machining ductile metals, Int. J. Mach. Tools Manuf. 51 (2011) 687–700.
[69] T. Mabrouki, F. Girardin, M. Asad, J.F. Rigal, Numerical and experimental study of dry cutting for an aeronautic aluminium alloy (A2024-T351), Int. J. Mach. Tools Manuf. 48 (2008) 1187–1197.

[70] M. Asad, F. Girardin, T. Mabrouki, J.F. Rigal, Dry cutting study of an aluminium alloy (A2024-T351): a numerical and experimental approach, Int. J. Mater. Form. Suppl. 1 (2008) 499–502.
[71] J. Sheikh-Ahmad, J.A. Bailey, Flow instability in the orthogonal machining of CP titanium, J. Manuf. Sci. Eng. 119 (1997) 307–313.
[72] Y.L. Bai, Thermo-plastic instability in simple shear, J. Mech. Phys. Solids 30 (1982) 195–207.
[73] P. Zhang, S.X. Li, Z.F. Zhang, General relationship between strength and hardness, Mater. Sci. Eng. A 529 (2011) 62–73.
[74] D. Umbrello, S. Rizzutia, J.C. Outeirob, R. Shivpuric, R. M'Saoubid, Hardness-based flow stress for numerical simulation of hard machining AISI H13 tool steel, J. Mater. Process. Technol. 199 (2008) 64–73.
[75] P.L.B. Oxley, Mechanics of Machining, Wiley, New York, 1989.
[76] M.E. Merchant, Mechanics of the metal cutting process I: orthogonal cutting and a type 2 chip, J. Appl. Phys. 16 (1945) 267–275.
[77] A. Molinari, X. Soldani, M.H. Miguélez, Adiabatic shear banding and scaling laws in chip formation with application to cutting of Ti–6Al–4V, J. Mech. Phys. Solids 61 (2013) 2331–2359.
[78] M. Calamaz, D. Coupard, F. Girot, A new material model for 2D numerical simulation of serrated chip formation when machining titanium alloy Ti–6Al–4V, Int. J. Mach. Tools Manuf. 48 (2008) 275–288.